

Final Analysis of ELAIS 15 μ m Observations: Method, Reduction and Catalogue

M. Vaccari^{1,2,3*}, C. Lari⁴, L. Angeretti⁵, D. Fadda⁶, C. Gruppioni^{7,8}, F. Pozzi⁵,
O. Prouton¹, H. Aussel⁹, P. Ciliegi⁸, A. Franceschini¹, E. González-Solares¹⁰,
F. La Franca¹¹, S. Oliver¹², I. Perez-Fournon¹³, M. Rowan-Robinson¹, S. Serjeant¹⁴
and P. Väisänen^{15,16}

¹ *Dipartimento di Astronomia, Università di Padova, Vicolo dell'Osservatorio 2, I-35122, Padova, Italy*

² *CISAS "G. Colombo", Università di Padova, Via Venezia 15, I-35131, Padova, Italy*

³ *Astrophysics Group, Blackett Laboratory, Imperial College, Prince Consort Road, London, SW7 2AZ, UK*

⁴ *Istituto di Radioastronomia, CNR, Via Gobetti 101, I-40122, Bologna, Italy*

⁵ *Dipartimento di Astronomia, Università di Bologna, Via Ranzani 1, I-40127, Bologna, Italy*

⁶ *Spitzer Science Center, MC 220-6, 1200 East California Boulevard, Pasadena, CA 91125, USA*

⁷ *Osservatorio Astronomico di Padova, INAF, Vicolo dell'Osservatorio 5, I-35122, Padova, Italy*

⁸ *Osservatorio Astronomico di Bologna, INAF, Via Ranzani 1, I-40127, Bologna, Italy*

⁹ *Institute for Astronomy, University of Hawaii, 2680 Woodlawn Drive, Honolulu, HI 96822, USA*

¹⁰ *Institute of Astronomy, University of Cambridge, The Observatories, Madingley Road, Cambridge, CB3 0HA, UK*

¹¹ *Dipartimento di Fisica, Università di "Roma Tre", Via della Vasca Navale 84, I-00146, Roma, Italy*

¹² *Astronomy Centre, Department of Physics & Astronomy, University of Sussex, Brighton, BN1 9QJ, UK*

¹³ *Instituto de Astrofísica de Canarias, Via Lactea S/N, E-38200, La Laguna, Spain*

¹⁴ *Centre for Astrophysics and Planetary Science, School of Physical Sciences, University of Kent, Canterbury, Kent, CT2 7NZ, UK*

¹⁵ *European Southern Observatory, Alonso de Cordova 3107, Casilla 19001 Santiago 19, Vitacura, Santiago, Chile*

¹⁶ *Observatory, P.O. Box 14, FIN-00014, University of Helsinki, Finland*

Accepted 2004 ? ?. Received 2004 ? ?; in original form 2004 ? ?

ABSTRACT

We present the Final Analysis of the European Large Area ISO Survey (ELAIS) 15 μ m observations, carried out with the ISOCAM instrument on board the Infrared Space Observatory (ISO).

The data reduction method, known as LARI method, is based on a mathematical model of the detector's behaviour and was specifically designed for the detection of faint sources in ISO-CAM/PHOT data. The method is fully interactive and leads to very reliable and complete source lists.

The resulting catalogue includes 1923 sources detected with $S/N > 5$ in the 0.5 – 100 mJy flux range and over an area of 10.85 deg² split into four fields, making it the largest non-serendipitous extragalactic source catalogue obtained to date from ISO data.

This paper presents the concepts underlying the data reduction method together with its latest enhancements. The data reduction process, the production and basic properties of the resulting catalogue are then discussed.

Key words: infrared: galaxies – galaxies: formation, evolution, active, starburst – cosmology: observations – methods: data analysis – catalogues.

1 INTRODUCTION

The Infrared Astronomical Satellite (IRAS, Neugebauer et al. 1984; Soifer et al. 1987) was extremely

successful in characterizing for the first time the global properties of the mid- and far-infrared sky, carrying out an all-sky survey at wavelengths of 12, 25, 60 and 100 μ m and leading to discoveries such as those of Luminous, Ultraluminous and Hyperluminous Infrared Galaxies (LIRGs, ULIRG and HLIRGs, respectively), a substantial popula-

* e-mail: m.vaccari@imperial.ac.uk

tion of evolving starbursts and the detection of large-scale structure in the galaxy distribution (Saunders et al. 1991).

Unfortunately, the IRAS view was typically limited to the very local Universe ($z \lesssim 0.2$), thus hampering statistical studies of infrared-luminous galaxies at cosmological redshifts. Only few sources were detected by IRAS at higher redshifts, typically ULIRGs magnified by gravitational lenses, like F10214+4724 ($z = 2.28$, Rowan-Robinson et al. 1991). In particular only about 1000 galaxies were detected all over the sky in IRAS 12 μm band. Infrared source counts based on IRAS data (Rowan-Robinson et al. 1984; Soifer et al. 1984) showed some marginally significant excess of faint sources with respect to no evolution models (Hacking et al. 1987; Franceschini et al. 1988; Lonsdale et al. 1990; Gregorich et al. 1995; Bertin et al. 1997), but not enough statistics and dynamic range in flux to discriminate between evolutionary scenarios were available.

Although conceived as an observatory-type mission, the Infrared Space Observatory (ISO, Kessler et al. 1996) was in many ways the natural successor to IRAS, bringing a gain of a factor ~ 1000 in sensitivity and ~ 10 in angular resolution in the mid-infrared. A substantial amount of ISO observing time was therefore devoted to field surveys aimed at detecting faint infrared galaxies down to cosmological distances. Such surveys were conceived as complementary in flux depth and areal coverage, allowing a systematic investigation of the extragalactic sky down to so far unattainable flux densities at both mid and far infrared wavelengths, whose results are summarized by Genzel and Cesarsky (2000). In particular, extragalactic 15 μm source counts determined with ISOCAM (Elbaz et al. 1999; Gruppioni et al. 2002) have revealed a significant departure from Euclidean slope within the 1 - 5 mJy flux range, which has been interpreted as evidence for a strongly evolving population of starburst galaxies.

The European Large Area ISO Survey (ELAIS, Oliver et al. 2000; Rowan-Robinson et al. 2003) was the most ambitious non-serendipitous survey and the largest Open Time project carried out with ISO, aimed at bridging the flux gap between IRAS all-sky survey and ISO deeper surveys. ELAIS observations mapped areas of about 12 deg^2 at 15 and 90 μm and smaller areas at 7 and 175 μm with the ISOCAM (Cesarsky et al. 1996, 7 and 15 μm) and ISOPHOT (Lemke et al. 1996, 90 and 175 μm) cameras. Most importantly, ELAIS 15 μm observations are the only ones allowing to sample the 1 - 5 mJy flux range, where most of the source evolution appears to take place.

Since the project approval, the ELAIS consortium, grown in time to a total of 76 collaborators from 30 European institutes, has undertaken an extensive program of ground-based optical and near-infrared imaging and spectroscopy. Thanks to such an extensive multi-wavelength coverage, the ELAIS fields have now become among the best studied sky areas of their size, and natural targets of ongoing or planned large-area surveys with the most powerful ground- and space-based facilities. Further details on ELAIS multi-wavelength observations and catalogues are presented in Rowan-Robinson et al. (2003). After the loss of the WIRE satellite, notwithstanding the observations at several infrared wavelengths soon to come from Spitzer and later from SOFIA and Herschel, ISO observations will remain a valuable database for many years to come. In particular, until

the advent of JWST, ELAIS 15 μm observations will provide a complementary view on three areas (S1, N1 and N2) which will be covered at different wavelengths as part of the Spitzer Wide-Area Extragalactic Survey (SWIRE, Lonsdale et al. 2003). Thus the need of reducing such data with the utmost care and provide the community with an agreed-upon legacy from the ELAIS project.

This paper presents the Final Analysis of ELAIS 15 μm observations, and is structured as follows. In Section 2 a brief description of the most relevant aspects of ELAIS 15 μm dataset is given. Section 3 describes the data reduction method and its improvements. In Section 4 the technique employed for flux determination and its results are presented. Section 5 details the results of the simulations that were carried out in order to assess the performance of the data reduction method and thus the quality of the resulting catalogue. In Sections 7 and 8, respectively, estimates of the achieved astrometric and photometric accuracy are given. Section 6 summarizes the identification of 15 μm sources in optical and near-infrared images, while Section 9 describes the procedure adopted to establish the catalogue photometric calibration. Finally, Section 10 describes gives a basic description of the catalogue contents.

2 THE ELAIS 15 μM DATASET

The ELAIS 15 μm main¹ dataset is made up of 28 rasters (ISO basic imaging observations), each covering an area of about $40' \times 40'$, divided into 4 fields, one (S1) in the southern hemisphere and three (N1, N2 and N3) in the northern one. Small superpositions at the boundaries and a limited degree of redundancy on portions of the fields give a total covered area of 10.85 deg^2 .

The fields were selected on the basis of their high ecliptic latitude ($|\beta| > 40^\circ$, to reduce the impact of Zodiacal dust emission), low cirrus emission ($I_{100\mu\text{m}} < 1.5 \text{ MJy/sr}$) and absence of any bright ($S_{12\mu\text{m}} > 0.6 \text{ Jy}$) IRAS 12 μm source. In Figure 1 the location on the sky of the survey fields is shown, overlaid on cirrus maps (COBE normalized IRAS maps of Schlegel et al. (1998)). Nearby IRAS sources with 12 μm fluxes brighter than 0.6 Jy are also plotted. The overall sky coverage, highlighting the position and redundancy of single rasters, is illustrated in Figure 2.

ELAIS 15 μm observations were carried out operating the ISOCAM instrument in raster mode using the LW3 filter. In this observing mode, the ISOCAM 32×32 pixel LW detector was stepped across the sky in a grid pattern, with about half detector width steps in one direction and the whole detector width steps in the other. Thus, reliability was improved as each sky position (apart from those at the boundaries of the raster region) was observed twice in successive pointings and overheads were reduced because each raster covered a large area ($\sim 40' \times 40'$). At each raster pointing (i.e. grid position) the detector was read out several

¹ Note that smaller sky regions observed with an higher redundancy as part of the ELAIS project, such as the S2 field (whose data reduction and analysis is described by Pozzi et al. (2003)), the X1,...,6 fields and the ultra-deep portion of the N1 field, which was observed ten times, are not considered in this work. See Oliver et al. (2000) for further details on these smaller fields.

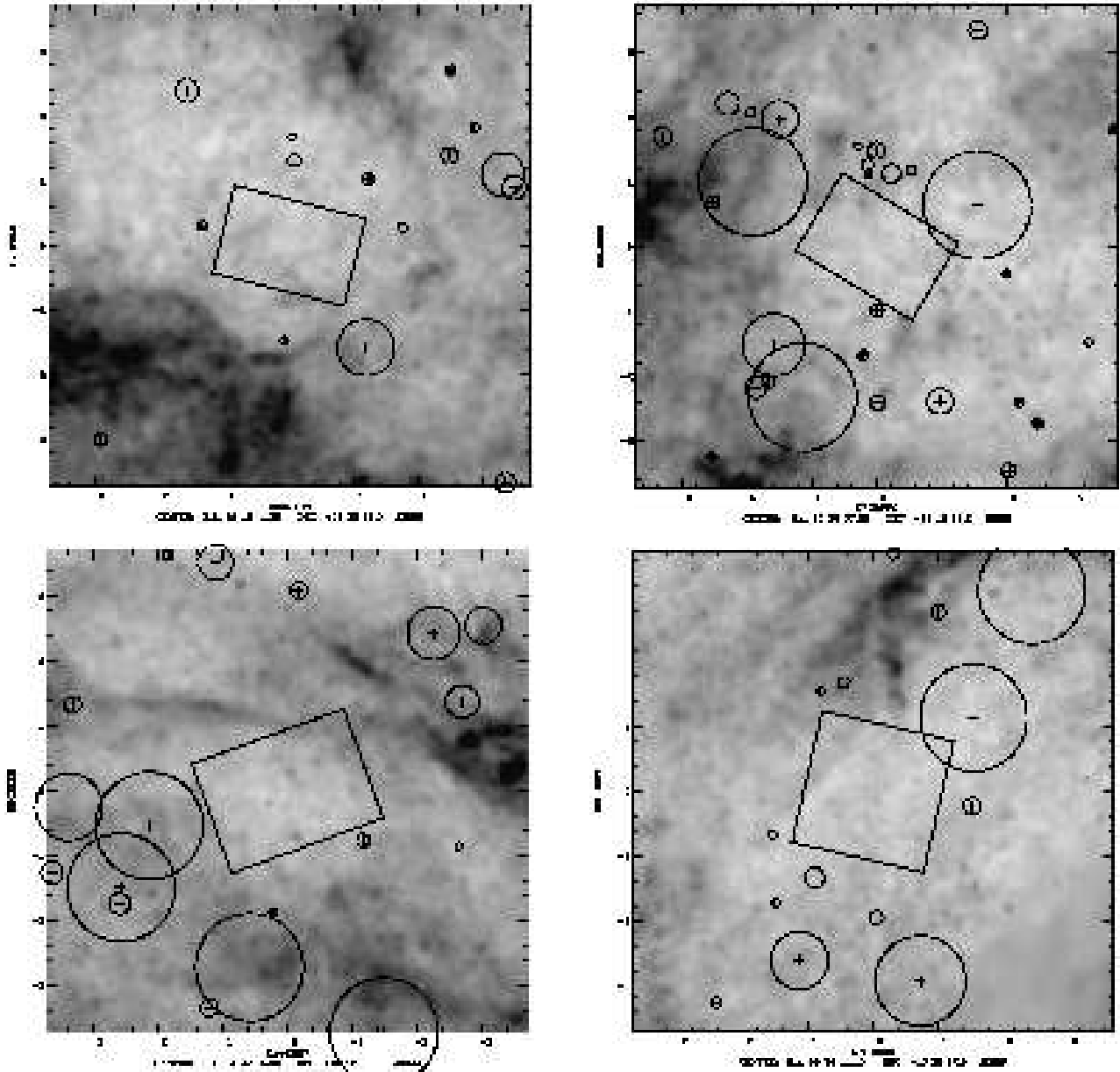


Figure 1. Sky Locations of ELAIS 15 μm Fields. From top left to bottom right: N1, N2, N3 and S1 areas. Greyscales indicate COBE normalized IRAS 100 μm intensity maps from Schlegel et al. (1998). IRAS sources with 12 μm fluxes brighter than 0.6 Jy are also drawn as circles with radii proportional to their fluxes

(typically 10) times, to increase the redundancy in order to be able to identify cosmic rays impacts and distinguish their severe effects on the electronics from real sources. Furthermore, on the raster first pointing, 80 readouts were carried out to allow the detector to approach stabilization. Table 1 describes the observation parameters for the LW3 observations, while Table 2 lists the fields and related ISO Data Archive filenames making up the dataset.

3 DATA REDUCTION

Reduction of data obtained with ISO instrumentation has always proved very difficult for a number of reasons. As far as ISOCAM observations carried out using its Long Wave-

length (LW) detector are concerned, the two most important instrumental phenomena one has to deal with are the qualitatively very different effects produced on the detector's electronics by the frequent and severe cosmic ray impacts, which have long been known and referred to as **glitches**, and its sizable transient behaviour after changes in the incident photon flux, which we will hereafter simply refer to as **transients**. In both cases, the cryogenic operational temperatures of the detector caused it to very slowly respond after these events. Lack of an accurate modeling of these effects can thus lead to spurious detections or errors in flux determination. In ELAIS 15 μm data reduction, the impact of these effects is increased by the instrumental parameters which were chosen in order to maximize the survey area. The short integration time (2.1 s \times 10 frames/pointing), the

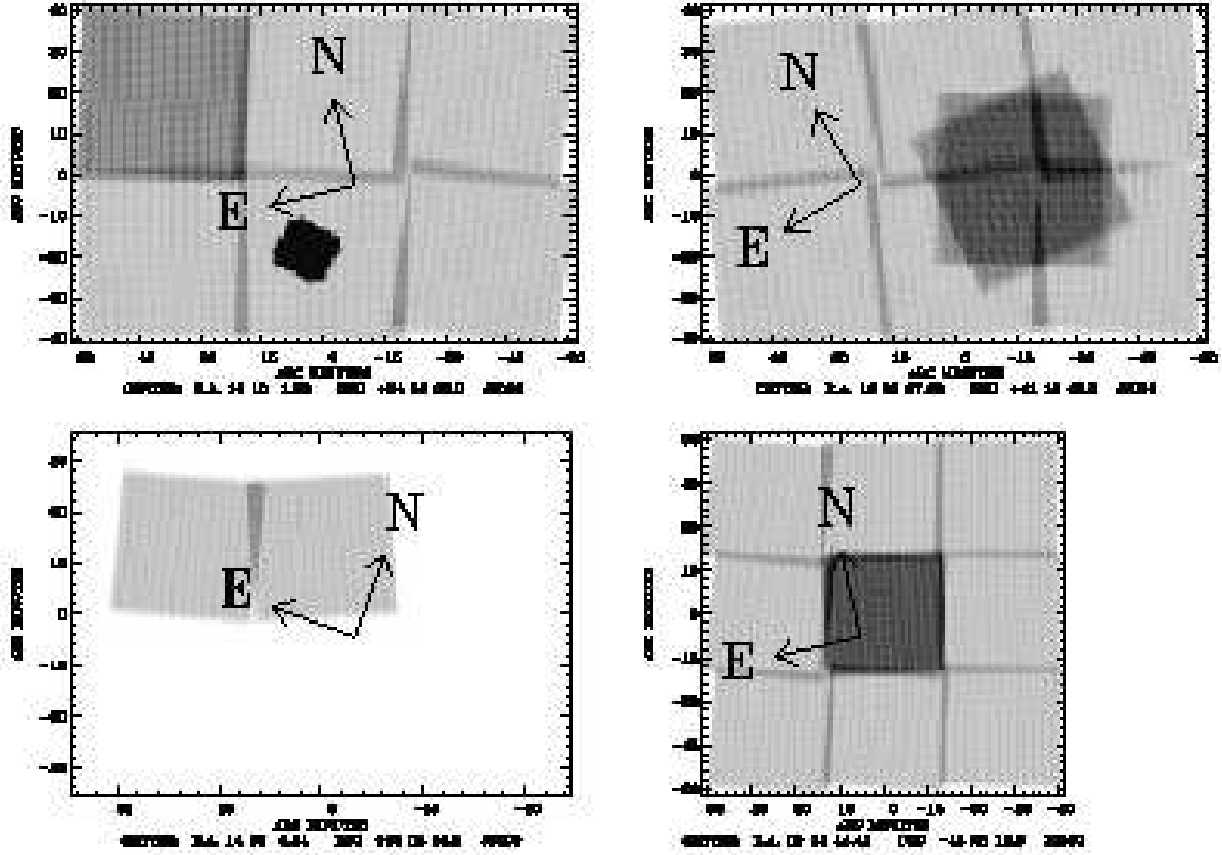


Figure 2. ELAIS 15 μm sky coverage. From top left to bottom right: N1, N2, N3 and S1 fields. Note that different fields are represented with a slightly different image scale.

Table 1. ELAIS ISOCAM LW3 Observation Parameters

Parameter	Value
Band λ_{eff}	14.3 μm
Band FWHM Range	12.0–18.0 μm
Detector gain	2 \dagger
Integration time	2 s
Number of exposures per pointing	10
Number of stabilization exposures	80
Pixel field of view	6''
Number of pixels	32 \times 32
Number of horizontal and vertical steps	28 , 14
Number of rasters (including repetitions)	28
Horizontal and vertical step sizes	90'' , 180''
Total area	10.85 deg ²

\dagger Except in "test" raster N2_R_A where gain was 1

large raster step (half the detector size along one axis and the whole detector size along the other one) and the large pixel size (6 arcsec) all contribute to reduce the redundancy and to increase the undersampling. Low redundancy and high undersampling, in turn, increase difficulties in distinguishing sources from strong glitches (low reliability) and in correctly determining source fluxes (low photometric accuracy).

Roughly speaking, glitches can be divided into three categories according to the way they shape the detector's

output signal, their decay time and influence on the pixel responsivity: glitches belonging to these different classes are respectively dubbed **common glitches**, **faders** and **dippers**. Slow decreases of the signal following cosmic ray impacts are called faders, while prominent reductions of the pixel responsivity very slowly recovering afterwards are called dippers. These two effects are believed to be associated with proton or α particle impacts on the detector, and have a fairly long lasting impact on pixel responsivities. Conversely, the much more frequent impacts of cosmic ray electrons produce common glitches characterized by a relatively fast decay time, lasting only a few readouts. Therefore, the number of frames affected by a single fader or dipper is much higher than in the case of a common glitch, the pixel responsivity taking from tens to hundreds of seconds to recover completely. However, common glitches are much more frequent than faders and dippers and, may all the same hamper the quality of data reduction. Thus, all kinds of glitches, if not correctly removed (or, more properly, corrected for), can lead to spurious detections, or **unreliability**, and to the loss of genuine sources, or **incompleteness**. On the other hand, transients all follow the same pattern, due to the fact that they arise from the non negligible time it takes for the output signal to reach the stabilization value after a change in the incident photon flux has taken place. The measured signal is thus always lower than the true one. Failing to model this time effect in data reduction can lead to a sys-

Table 2. ELAIS 15 μm Fields. Field Name, Raster Name, ISO Data Archive (IDA) Official Filename and Raster Centre Coordinates

Field	Raster	IDA	RA (J2000)	Dec (J2000)
S1	S1_1	23200251	00 30 25.40	-42 57 00.3
	S1_2	23200353	00 31 08.20	-43 36 14.1
	S1_3	41300955	00 31 51.90	-44 15 27.0
	S1_4†	23300257†	00 33 59.40	-42 49 03.1
	S1_5_A	23300459	00 34 44.40	-43 28 12.0
	S1_5_B	77500207	00 34 44.40	-43 28 12.0
	S1_5_C	78502406	00 34 44.40	-43 28 12.0
	S1_6‡	41001161‡	00 35 30.40	-44 07 19.8
	S1_7	40800663	00 37 32.50	-42 40 41.2
N1	S1_8	40800765	00 38 19.60	-43 19 44.5
	S1_9	41001867	00 39 07.80	-43 58 46.6
	N1_1	30200101	16 15 01.00	+54 20 41.0
	N1_2_A§	30400103§	16 13 57.10	+54 59 35.9
	N1_2_B	67200103	16 13 57.10	+54 59 35.9
	N1_3	30500105	16 10 34.90	+54 11 12.7
	N1_4	30600107	16 09 27.00	+54 49 58.7
	N1_5	31000109	16 06 10.80	+54 01 08.0
	N1_6	30900111	16 04 59.00	+54 39 44.3
N2	N2_1	50200119	16 32 59.80	+41 13 33.2
	N2_2	51100131	16 34 44.50	+40 38 45.0
	N2_3	50000723	16 36 05.50	+41 33 11.8
	N2_4	50200225	16 37 48.90	+40 58 13.1
	N2_5	50100727	16 39 13.80	+41 52 31.6
	N2_6	50200429	16 40 55.50	+41 17 22.7
	N2_R_A	11600721	16 35 45.00	+41 06 00.0
	N2_R_B	77900101	16 35 45.00	+41 06 00.0
N3	N3_3	42500237	14 29 38.30	+33 24 49.6
	N3_5	43800341	14 32 38.20	+33 11 10.3

† Originally flagged as "Telemetry Drops" in observation logs

‡ Originally flagged as "Unknown Quality" in observation logs

§ Originally flagged as "Aborted" in observation logs

tematic underestimation of source fluxes. For these reasons, the data cleaning and modeling is an extremely delicate process requiring great care in order to produce highly reliable sky maps and source lists.

While it was variously demonstrated that it is possible, at least to a certain extent, to describe the detector's behaviour adopting some physical model, the large number of readouts involved in raster observations and the peculiar nature and strength of noise patterns also require efficient and robust algorithms to be developed so as to make the actual data reduction undertaking feasible in a nearly-automatic way.

A number of data reduction methods has thus been developed and tested, mostly on deep fields (e.g. the PRETI method by Starck et al. (1999) and the Triple Beam Switch method by Désert et al. (1999)). Unfortunately, such methods did not prove completely reliable on shallower fields, leading to a high number of false detections. Besides, these methods suffered from the lack of an efficient way to interactively check the quality of the data reduction when needed. The Preliminary Analysis of ELAIS 15 μm data (Serjeant et al. 2000) was thus carried out adopting a more traditional approach involving the corroboration of automated detections through visual inspection by different observers.

The data reduction described in this paper was car-

ried out using the LARI method (Lari et al. 2001, 2003), a new technique developed to overcome these difficulties and provide a robust interactive technique for the reduction and analysis of ISOCAM and ISOPHOT data, particularly suited for the detection of faint sources and thus for the full exploitation of their scientific potential. The method was variously refined, and significantly better results are now obtained, with respect to the technique used in Lari et al. (2001) for the reduction of the S1 field, so that a thorough re-reduction of all ELAIS fields seemed appropriate and was thus carried out. As before, data reduction is carried out within an IDL environment using mostly purpose-built routines, exploiting CAM Interactive Analysis (Ott et al. 2001, CIA,) software for basic operations only.

3.1 The Model

The LARI method describes the sequence of readouts, or time history, of each pixel of ISOCAM LW3 detector in terms of a mathematical model for the charge release towards the contacts. Such a model is based on the assumption of the existence, in each pixel, of two charge reservoirs, a short-lived one Q_b , also known as **breve**, and a long-lived one Q_l , also known as **lunga**, evolving independently with a different time constant and fed by both the photon flux and the cosmic rays. The model is fully charge-conservative, i.e. no decay of accumulated charges is considered, except towards the contacts, and thus the observed signal S is related to the incident photon flux I and to the accumulated charges Q_b and Q_l by the

$$S = I - \frac{dQ_{tot}}{dt} = I - \frac{dQ_b}{dt} - \frac{dQ_l}{dt}, \quad (1)$$

where the evolution of these two quantities is governed by the same differential equation, albeit with a different efficiency e_i and time constant a_i

$$\frac{dQ_i}{dt} = e_i I - a_i Q_i^2 \quad \text{where } i = b, l, \quad (2)$$

so that

$$S = (1 - e_b - e_l) I + a_b Q_b^2 + a_l Q_l^2. \quad (3)$$

The values of the parameters e_i and a_i depend on the detector's physics, and are thus assumed to depend on the exposure time of a given observation and on the stabilization background level of a given pixel, according to the relation

$$a_i = \frac{t}{t_0} \sqrt{\frac{S}{S_0}} a_{i,0}, \quad (4)$$

where $a_{i,0}$ is the value of a_i relative to a reference exposure time t_0 and average signal level S_0 . In practice, an additive offset signal attributable to thermal dark current (a component which is otherwise removed in standard dark current subtraction), is actually added to both S and I in the equation above when it is estimated to be important, i.e. in the rare cases when the deepest dippers' depth otherwise exceeds 10% of the stabilization background level.

3.2 Pipeline

Data reduction begins with a preliminary **pipeline** incorporating all necessary steps in order to prepare the data for

the temporal fitting procedure which is the critical step of the LARI method.

Raw data downloaded from the ISO Data Archive are first imported into the IDL `raster` structure containing all observational information using CIA routines. Likewise, dark current subtraction and conversion from ADU to ADU/gain/s are carried out using CIA. Then a dedicated IDL structure called `liscio` is built in order to contain not only all `raster` information but also all ancillary arrays needed in order to carry out the following reduction.

At this stage potential glitches are identified through a two-step median filtering process of each pixel time history, or **deglitching**. Then a separate routine determined the stabilization background (or global background, as opposed to the local background described below) and the aforementioned offset signal. Such routine was carefully devised to filter out in so far as possible long-term effects such as stabilization, faders and dippers and thus provide a reliable estimate of these two parameters the fitting procedure is particularly sensitive to. The same routine also identifies the few potential bright sources which at times the fit failed to recognize by itself, which are then interactively checked by eye to assess their reliability.

3.3 Fitting

The signal as a function of time is finally processed independently for each pixel. The fitting procedure models the transients attributable to changes in incident flux and the features on both short and long time scales produced by cosmic ray impacts on the time history, modeling glitches as discontinuities in the charge release. As seen in Section 3.1, the same values for the e_i and a_i parameters are used for all pixels, apart from the scaling of the a_i according to the exposure time and the stabilization background level, leaving as free parameters only the charges at the beginning of the observation and at the "peaks" of glitches.

Glitches from nearby pixels are also considered when their height is substantially (i.e. 20 times) higher than the chosen threshold. The fitting algorithm starts with the strongest potential glitches identified in pipeline deglitching, assumes discontinuities at these positions and tries to find a fit to the time history that satisfies the model assumed to describe the solid-state physics of the detector. If no acceptable fit is found, the next fainter glitch is considered as a potential discontinuity, and so on. Iteration of the fitting procedure is interrupted when either a satisfactory (typically 0.2 ADU/gain/s) data-model rms deviation is achieved or the maximum number of allowed iterations is reached.

At this stage the code estimates several quantities needed to build the sky maps on which source extraction will then be performed. All of these quantities are "recovered" from glitches, i.e. already take into account discontinuities in charge release assumed to describe glitches during fit, and their list includes:

- the charges stored into the **breve** and **lunga** reservoirs at each readout.
- the local background, i.e. the signal to be expected on the basis of the previously accumulated charges if only the stabilization background were hitting the detector.

- the model signal, produced by the incident flux coming from both the stabilization background and detected sources.

- the **"unreconstructed"** signal, i.e. the detected flux recovered from glitches but not from transients. This is computed as the difference between the measured signal and the local background.

- the **"reconstructed"** signal, i.e. the detected flux recovered not only from glitches but also from transients associated with changes in incident flux.

For the sake of clarity, one must emphasize here the differences between the two kinds of signals (and the corresponding fluxes and sky maps they will finally turn into) defined above, namely **unreconstructed** and **reconstructed** signals. Both quantities take into account the effects of the stabilization background and glitches on the detector, and their values are thus expected to be negligible if a source is not illuminating the pixel at the given pointing. The difference between the two quantities only appears when an additional signal the code is not able to model otherwise (i.e. as the effect of a glitch) is detected and attributed to a source of a given flux. The code then models the transients expected from such an additional flux and "reconstructs" the signal one would detect if they did not affect the detector, i.e. if its response were instantaneous. In other words, unreconstructed signals do not take into account the effects of this modeling of changes in incident flux, thus representing the effective charge collected during the exposure, whereas reconstructed signals recover the charge "loss" due to the slow detector response. Therefore, the former are systematically lower than the latter. Actually, simulations show that the code is not actually able to properly model transients below a certain intensity threshold, thus suggesting the use of unreconstructed signals only to carry out further processing.

Figure 3 shows how a successful fit is able to describe cosmic-ray-induced violent changes in the signal level and thus recover useful information (specifically, source fluxes) from the pixel time history. Panels a) and b) show two examples of how glitches (a fader and a dipper, respectively) are described as discontinuities in the signal level slowly recovering towards the stabilization background, while panels c) and d) show how sources are detected even on the top of strong glitches. The solid line represents the observed data, the short-dashed line the best-fit model and the long-dashed line the detected (unreconstructed) flux. The dot-dashed line finally represents the stabilization background

3.4 Interactive Analysis

After running the fitting procedure on the time history of all pixels making up a raster, the interactive analysis of fitting results is carried out, looking in detail at portions of the time history that were not well-fit by the automated analysis. The details of the interactive analysis process need to be tuned to the quality of the specific raster under consideration. In particular, the choice of thresholds in interactive checks is closely related with observing parameters such as the exposure time but also with the varying frequency and severeness of cosmic ray impacts. Generally speaking, more careful checks could be profitably carried out on intrinsically higher-quality data. On the other hand, it is desirable to en-

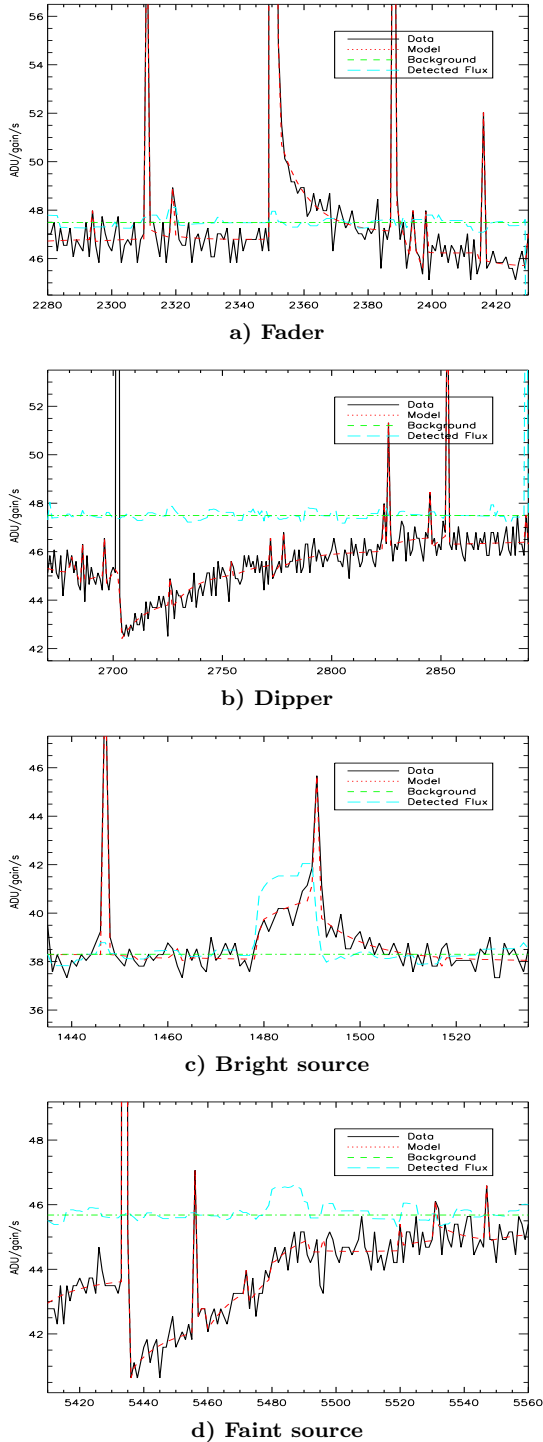


Figure 3. Different troublesome situations in pixel time histories: a) Recovery of stabilization background level after a fader b) Recovery of stabilization background level after a dipper c) Detection of a bright source hidden by a strong common glitch d) Faint source hidden by the recovery of the stabilization background level after a dipper. Here "Background" stands for stabilization background and "Detected Flux" for reconstructed flux.

sure the most uniform data reduction as practicable. It was thus decided to adopt a common trade-off between the data quality of all rasters making up our dataset and to apply it to all rasters.

As a first step, fitting failures flagged by substantial data-model rms deviations (higher than 0.23 ADU/gain/s) or negative signals (lower than -0.6 ADU/gain/s) are checked. Then all sizeable signal excesses (unreconstructed signals higher than 0.5 ADU/gain/s) are individually inspected. Whenever the need arises, a further fit extending to the whole pixel time history or to a smaller portion of it is carried out. Particularly noisy regions or very strong individual features completely preventing data reduction are masked.

The massive work of interactive analysis is carried out with an easy-to-use IDL widget-based Graphical User Interface, a screenshot of which is shown in Figure 4, which allows any kind of operation that could be necessary: data visualization and browsing, glitch addition and correction, time history masking and re-fitting. Such software is the main factor allowing the increase in the volume and quality of the obtained catalogues with respect to Lari et al. (2001).

3.5 Mapping

Once a satisfactory fit is obtained over the whole time history for all pixels, one can proceed to the generation of sky maps and to source extraction. After masking glitches and other noisy parts of the time history identified during Interactive Analysis, flat-fielding is carried out and a signal estimate for each raster pointing is computed by averaging all readouts relative to that pointing. The result is converted from ADU/gain/s to mJy using ISOCAM LW3 standard sensitivity $1 \text{ mJy} = 1.96 \text{ ADU/gain/s}$. The "images" thus computed relative to all raster pointings are then projected onto a $2'' \times 2''$ pixel sky map adopting nominal astrometric information and using a new mapping technique optimized to partly overcome the severe PSF undersampling due to the large pixel size adopted in observations. Here and in the following, all necessary projections are carried out using the `projection` C++ code included in CIA. In so doing, ISOCAM severe field distortion (Okumura 2000) was taken into account as determined by Aussel et al. (1999), whereas PSF modeling followed the prescriptions given by Okumura (1998) for stellar PSFs but adopting a spectrum of the form $f_\nu = \text{constant}$, i.e. a closer match to the expected galaxy spectrum than the Rayleigh-Jeans form used for stellar spectra. The resulting PSF is larger than the one computed for stars.

Following this procedure, both unreconstructed and reconstructed sky maps are produced. In both cases, two ancillary maps are also constructed. The sky coverage (or "NPIX") map contains the number of independent "images" added together to obtain a pixel value in the final map. On the other hand, the noise (or "RMS") map contains the estimate of the root mean square noise of each single pixel in the final map, computed by scaling the overall root mean square noise of the map as measured at its centre according to the inverse square root of the noise map.

Source detection is then performed on unreconstructed sky maps. First, all pixels above a conservatively low flux threshold (60 μ Jy) are selected, then the IDL Astron-

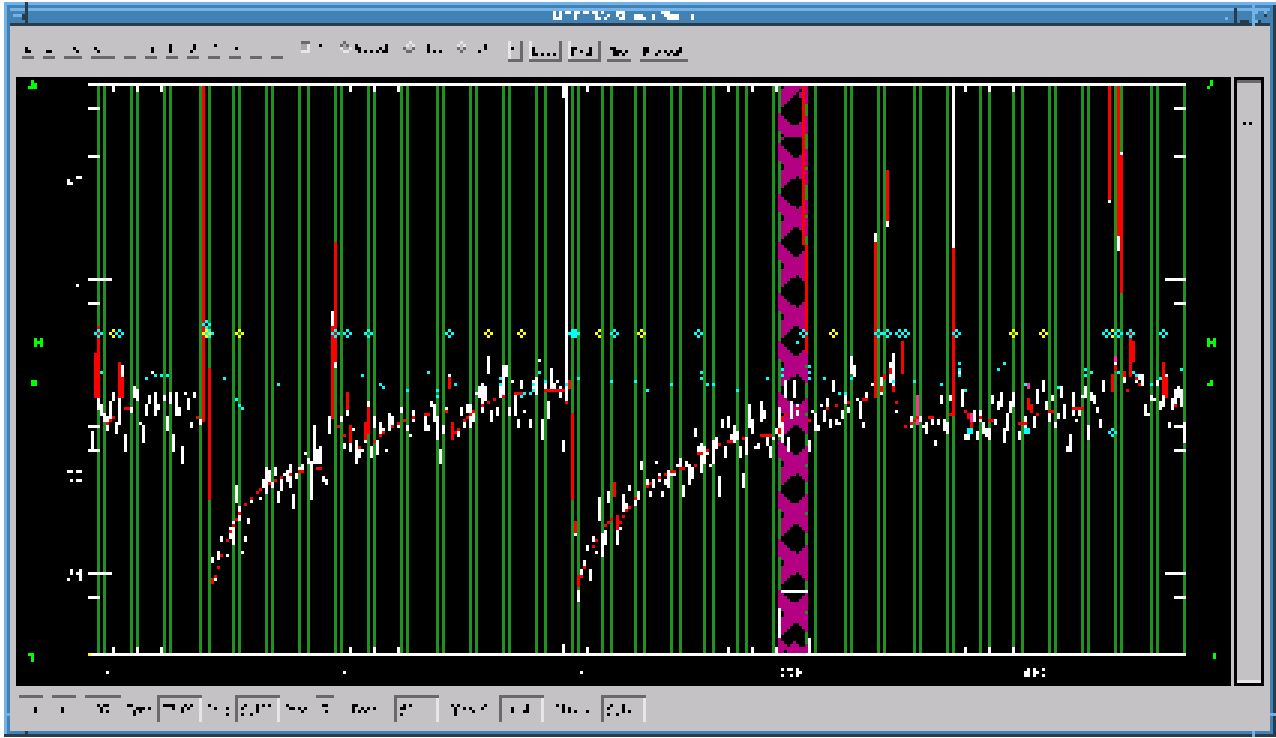


Figure 4. A screenshot of the IDL widget-based Graphical User Interface used to carry out interactive analysis.

omy User's Library `find` routine (based on DAOPHOT's homonymous routine, particularly suited for the detection of point-like sources in crowded fields) is used to identify positive brightness perturbations around these pixels and return their peak flux, S/N , centroid and shape parameters such as roundness and sharpness.

At this stage, further interactive checks are performed on all sources detected with a S/N greater than 5 to assess their reliability. More specifically, sources detected on the sky map are projected back onto the time history to identify all raster pointings where the source is supposed to contribute a significant signal. Then all these pointings are individually checked and, if necessary, refitted, to improve the fit and thus recover lost signals or remove spurious ones. The overall results of these further checks are an increased reliability and an improved astrometric and photometric accuracy.

3.6 Mosaicing

Up to this stage, all rasters are reduced and processed individually. However, in order to fully exploit the limited redundancy of the observations, a technique to build a mosaic out of rasters covering the same field was devised. This is carried out as follows. Once the reduction of all rasters of interest is completed according to the above procedure, the necessary corrections to nominal astrometry are determined as the median offset between ELAIS source positions expressed with respect to nominal astrometry and the positions of USNO A2.0 sources found in the field. This is done through a two-step process. First, the two catalogues are cross-correlated, assigning to each ELAIS sources its closest

USNO association. The median of the positional differences thus determined, excluding ELAIS sources with no USNO association within 12 arcsec, is computed and assumed as a first-order correction to ELAIS source positions. The cross-correlation procedure is then repeated to calculate a second-order astrometric correction in exactly the same way, the only difference being that ELAIS sources with no USNO identification within 3 times the root mean square deviation of ELAIS-USNO association distance are also excluded during this second step. The sum of the two corrections is assumed as the raster offset with respect to nominal astrometry, and the root mean square deviation of ELAIS-USNO distances as the error in the offset determination. Deviations from nominal astrometry have long been known to be significant in ISO raster observations, and this is confirmed by our results, which are summarized in Table 3. Most total offsets are greater than or of the order of the pixel field of view size (6 arcsec), whereas associated errors have a mean value of 0.39 arcsec. The small errors are not only due to the careful data reduction, but also to the large number of ELAIS sources, and largely contribute to the very good overall astrometric accuracy quantified in Section 7.

A common mosaic grid is then built on which different rasters belonging to the same field are projected taking into account astrometric offsets. Mapping, source extraction, projection of sources detected with a S/N greater than 5 back on time history and interactive checks are furtherly performed on this mosaic sky map exactly as on single raster sky maps. The quality of data reduction is thus improved through cross-checks of sources detected on different rasters, increasing reliability and completeness in repeatedly observed regions and partly overcoming the

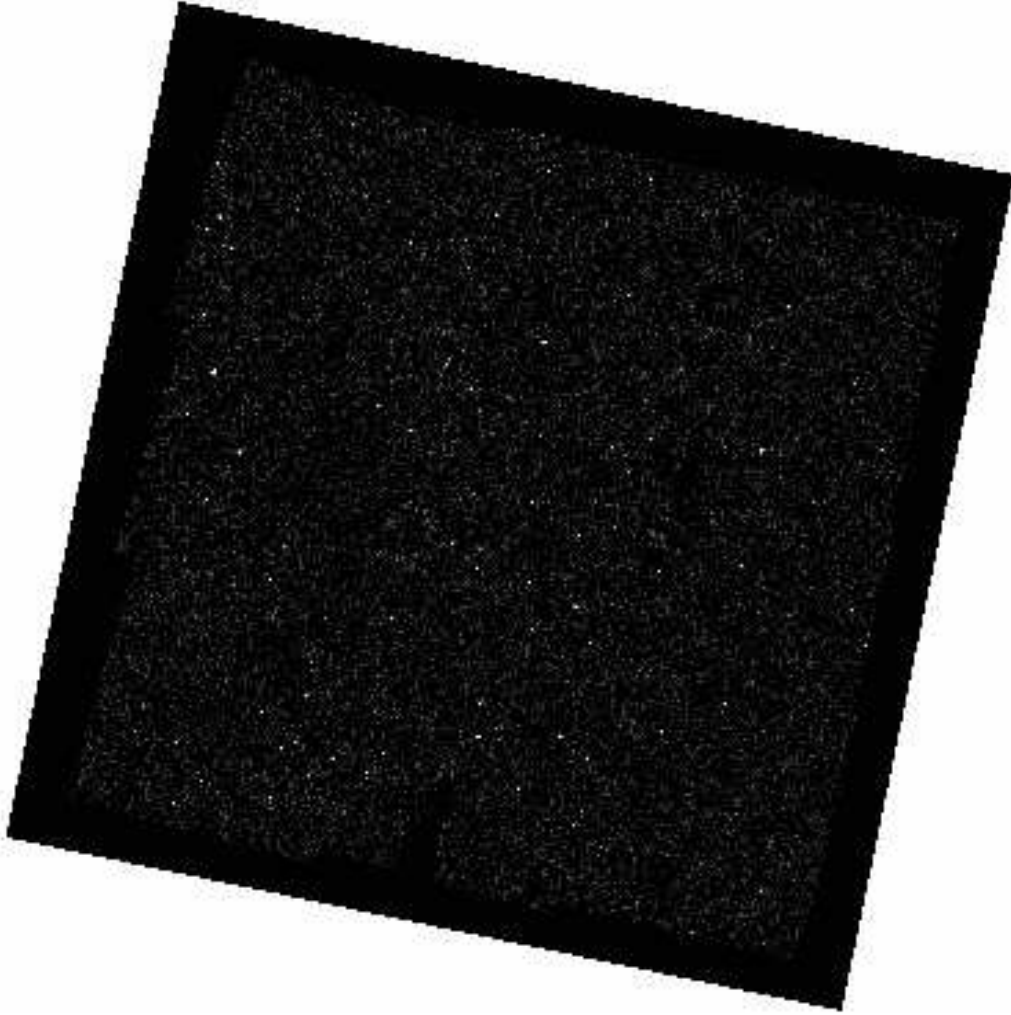


Figure 5. S1 Field S/N Sky Map. Image size is $2.335 \times 2.335 \text{ deg}^2$. North is up and East is left.



Figure 6. N3 Field S/N Sky Map. Image size is $0.866 \times 1.454 \text{ deg}^2$. North is up and East is left.

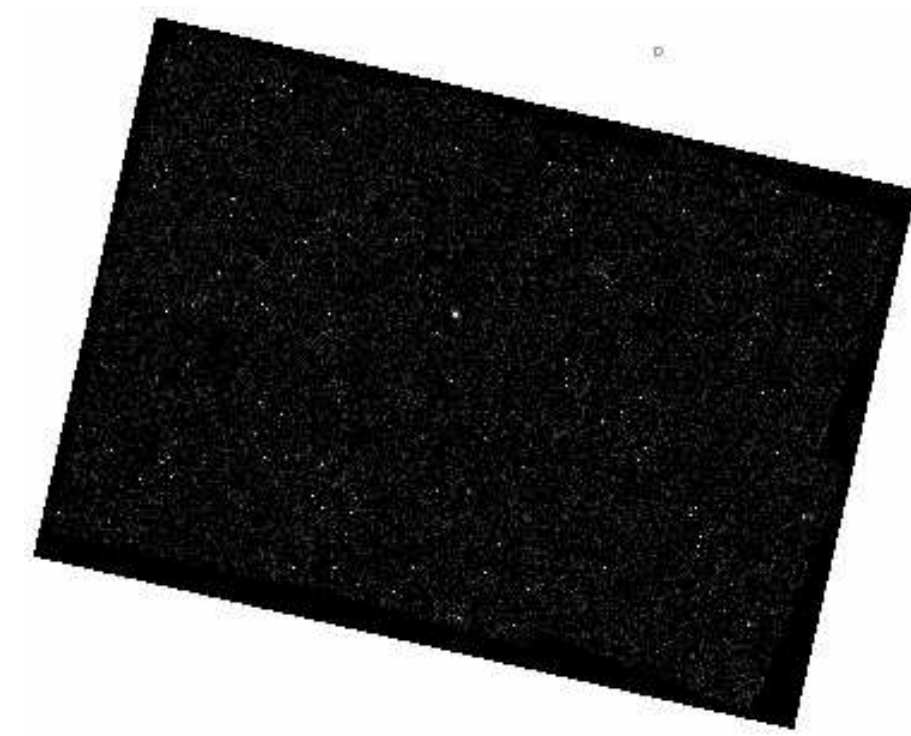


Figure 7. N1 Field S/N Sky Map. Image size is $1.514 \times 2.134 \text{ deg}^2$. North is up and East is left.



Figure 8. N2 Field S/N Sky Map. Image size is $1.559 \times 2.117 \text{ deg}^2$. North is up and East is left.

otherwise severe problems at raster boundaries. The final S/N sky maps of the four fields are shown in Figures 5, 6, 7 and 8. Typical noise levels are between 20 and 30 $\mu\text{Jy/pixel}$. Such maps, together with noise and sky coverage maps, will soon be available in FITS format at <http://astro.imperial.ac.uk/~vaccari/elais>.

4 AUTOSIMULATION

Even after a very careful reduction, flux determination is a very delicate process owing to the interplay of different factors, the most important being mapping effects related to PSF undersampling, detector's transients and other trends due to the limits of the adopted reduction method. Mapping effects are particularly tricky, since they determine the way one obtains source total fluxes from corresponding peak fluxes measured on sky maps by source detection software. Clearly, the conversion factor between these two quantities is very much dependent on the actual source position with respect to the centre of the pixel, a source total flux being nearer to its peak flux the nearer the source is to the center of the sky map pixel. The technique we developed, which we called **autosimulation**, was conceived to model and insofar as possible take into account mapping and data reduction effects on flux determination by first constructing both real and theoretical (i.e. noise-free) sky maps, and then use the latter ones to correct fluxes obtained from the former ones. Autosimulation consists in simulating sources, on top of noise-free maps, at each position where a source was actually detected (or, for simulations described in Section 5, at their randomly generated positions), calculating the ratio between peak and total flux for the simulated source on such theoretical sky maps, and converting the measured peak flux of the real source to its total flux using such ratio. Source simulation is carried out in a straightforward way using the same mathematical model the LARI method is based on, thus also allowing to verify its predictions.

In order to describe how autosimulation works in some greater detail, a few definitions and relations which will also be useful to discuss the results of simulations described in Section 5 must be summarized:

- f_s is the measured peak flux obtained from real (i.e. containing glitches, noise and transients) sky maps. Its value therefore depends on mapping effects, transients and the adopted data reduction method;
- f_0 is the "theoretical" peak flux obtained from simulated (i.e. containing neither glitches nor noise but taking into account source transients) maps. Its value depends on mapping effects and transients only.
- f_{sr} and f_{0r} are analogous to f_s and f_0 but are built from reconstructed maps, thus recovering the effects of transients. As already mentioned, this strictly holds above a certain flux threshold only, where the values of these quantities actually cease to depend on transients.

The correction factor for mapping effects is computed as follows. A simulated source is generated on each position where a real source was actually detected, assuming a total flux $S_0 = f_s / \langle f_s/S \rangle_{sim}$ based on the measured peak flux f_s and on the average peak flux / total flux ratio $\langle f_s/S \rangle_{sim} = 0.216$ obtained from simulations (see Section 5 and Figure 13).

Then the flux estimate corrected for mapping effects is computed as $S = (f_s/f_0) S_0$. Source simulation is carried out using the same model for charge release adopted in fitting the data. In so doing, however, autosimulation does not correct for more subtle and elusive effects arising from data reduction, such as flux loss due to bad fits, which can only be assessed through simulations. This is described in Section 5.1.

Such a procedure provides reliable flux estimates which are well compatible with estimates obtained through conventional aperture photometry for most sources, but is clearly non-optimal when dealing with extended sources. For these, as well as for a few very close or blended sources, aperture photometry usually provides a better estimate of the source flux. After correcting fluxes for mapping effects, potentially extended sources are therefore identified through both visual inspection of sky maps and the calculation of parameters connected to source extension. Sources flagged by these criteria (totalling 67 out of 1923 making up the catalogue, or 3.5%) were then individually treated, aperture photometry with a suitable aperture radius was carried out and the result was adopted as their most reliable flux estimate. As to the overall performance of the autosimulation process when compared with aperture photometry, autosimulated fluxes and their counterparts calculated through aperture photometry are compared for all sources in Section 5.3.

5 SIMULATIONS

Due to the peculiar nature of ISO data and of the reduction method employed, it is important to carefully test the performance of the latter on "ideal" data and sources. In particular, systematic effects on flux estimates related to the data reduction method can only be probed by these means. Due to the strong peculiarities of our dataset, which is characterized by several noise features on different time scales, only real data can effectively be taken as representative of instrumental behaviour. Therefore, the effects of artificial sources must be somehow simulated on the top of real pixel time histories, and data reduction must then be carried out exactly as done for real sources. Source confusion in the field is thus slightly increased, but this effect is not critical for ELAIS data. The LARI Method is based on a physical model of the detector's behaviour, so can make straightforward predictions of the effect on the detector of the additional photons from simulated sources. On this basis, an extensive set of simulations was carried out to assess the effects on flux estimates and the overall performance of data reduction in a statistically meaningful way. The S1 field was chosen for this purpose as the most representative, being the largest and including both regions observed only once and repeatedly observed regions (hereafter, **non-repeated** and **repeated** regions, respectively), therefore allowing to assess the differences in performance warranted by higher redundancy.

Simulations were carried out as follows. First a set of $N = 600$ random sky positions (excluding regions near to real sources, mosaic sky map boundaries and masked regions of mosaic sky map, i.e. preventing simulated sources to appear nearer than 15 arcsec to any of these regions) was generated. Then a logarithmically uniform flux distribution

Table 3. Astrometric offsets of ELAIS rasters. Corrections to ISO nominal astrometry as determined through cross-correlation between ELAIS and USNO A2.0 source lists.

Raster	Nominal Position		RA (")	Dec (")	Total (")
	RA (J2000)	Dec (J2000)	offset \pm error	offset \pm error	offset \pm error
S1_1	00 30 25.40	-42 57 00.3	-2.06 \pm 0.40	-4.46 \pm 0.38	4.91 \pm 0.55
S1_2	00 31 08.20	-43 36 14.1	-3.24 \pm 0.22	+6.86 \pm 0.29	7.59 \pm 0.36
S1_3	00 31 51.90	-44 15 27.0	+1.57 \pm 0.29	-7.75 \pm 0.33	7.91 \pm 0.44
S1_4	00 33 59.40	-42 49 03.1	+0.23 \pm 0.22	-4.01 \pm 0.27	4.02 \pm 0.35
S1_5_A	00 34 44.40	-43 28 12.0	-3.50 \pm 0.23	+9.63 \pm 0.27	10.24 \pm 0.35
S1_5_B	00 34 44.40	-43 28 12.0	-0.52 \pm 0.21	-8.10 \pm 0.26	8.12 \pm 0.33
S1_5_C	00 34 44.40	-43 28 12.0	-3.04 \pm 0.24	+5.34 \pm 0.29	6.14 \pm 0.38
S1_6	00 35 30.40	-44 07 19.8	+0.60 \pm 0.43	-7.14 \pm 0.24	7.17 \pm 0.49
S1_7	00 37 32.50	-42 40 41.2	+1.26 \pm 0.22	-5.62 \pm 0.38	5.76 \pm 0.44
S1_8	00 38 19.60	-43 19 44.5	+0.72 \pm 0.22	-5.31 \pm 0.24	5.36 \pm 0.36
S1_9	00 39 07.80	-43 58 46.6	-2.34 \pm 0.19	+4.61 \pm 0.23	5.17 \pm 0.30
N1_1	16 15 01.00	+54 20 41.0	+1.96 \pm 0.34	-9.34 \pm 0.21	9.54 \pm 0.40
N1_2_A	16 13 57.10	+54 59 35.9	+3.27 \pm 0.31	-9.48 \pm 0.22	10.02 \pm 0.38
N1_2_B	16 13 57.10	+54 59 35.9	+4.17 \pm 0.23	-7.89 \pm 0.15	8.92 \pm 0.27
N1_3	16 10 34.90	+54 11 12.7	-1.04 \pm 0.42	-6.18 \pm 0.25	6.27 \pm 0.49
N1_4	16 09 27.00	+54 49 58.7	+4.60 \pm 0.44	-6.71 \pm 0.23	8.14 \pm 0.50
N1_5	16 06 10.80	+54 01 08.0	-8.90 \pm 0.27	+3.77 \pm 0.18	9.67 \pm 0.32
N1_6	16 04 59.00	+54 39 44.3	-8.71 \pm 0.32	+3.88 \pm 0.22	9.54 \pm 0.39
N2_1	16 32 59.80	+41 13 33.2	-4.68 \pm 0.23	+7.18 \pm 0.21	8.57 \pm 0.31
N2_2	16 34 44.50	+40 38 45.0	+2.93 \pm 0.27	-2.87 \pm 0.27	4.10 \pm 0.38
N2_3	16 36 05.50	+41 33 11.8	-5.50 \pm 0.46	+7.30 \pm 0.37	9.14 \pm 0.59
N2_4	16 37 48.90	+40 58 13.1	-5.36 \pm 0.24	+7.46 \pm 0.21	9.19 \pm 0.32
N2_5	16 39 13.80	+41 52 31.6	-5.43 \pm 0.29	+7.32 \pm 0.24	9.11 \pm 0.38
N2_6	16 40 55.50	+41 17 22.7	-2.45 \pm 0.28	+2.32 \pm 0.24	3.38 \pm 0.37
N2_R_A	16 35 45.00	+41 06 00.0	+1.29 \pm 0.33	+6.01 \pm 0.21	6.15 \pm 0.39
N2_R_B	16 35 45.00	+41 06 00.0	+5.91 \pm 0.34	+4.24 \pm 0.22	7.27 \pm 0.40
N3_3	14 29 38.30	+33 24 49.6	-1.39 \pm 0.30	-3.44 \pm 0.16	3.71 \pm 0.34
N3_5	14 32 38.20	+33 11 10.3	-0.17 \pm 0.31	-3.52 \pm 0.24	3.52 \pm 0.39

covering the range between a lower limit $S_l = 0.5$ mJy and an upper limit $S_u = 4.0$ mJy

$$S_n = S_l \left(\frac{S_u}{S_l} \right)^{n/N} \quad \text{for } n = 0, N-1 \quad (5)$$

was coupled with the random positions above to characterize the set of simulated sources. Following the same procedure, 100 more sources were simulated (adopting a flux distribution following the same analytical formula but covering the 0.35–3.5 mJy flux range) in the repeated regions of the field, thus increasing the otherwise low number of simulated sources in these regions. All 700 sources were then projected from their sky position back onto the pixel time history, simulating their effects as superposed on glitches and noise characterizing the real data. In so doing, all portions of time history where simulated sources were predicted to give a sizeable additional signal were identified. The fitting procedure was thus re-run on these regions only, and all steps of data reduction and flux determination were then carried out on simulated sources exactly as described in Section 3 for real sources. At this stage the positions and fluxes of simulated sources that had been detected with a S/N greater than 5 were compared with the input values to calibrate and evaluate the performance provided by our data reduction method in different respects. The overall number of simulated and detected sources is given in Table 4, whereas the following Sections detail all relevant aspects of simulations, apart from the completeness estimates which

Table 4. Number of Simulated and Detected Sources. Total figures are given together with those for non-repeated and repeated regions.

	Non-Repeated	Repeated	Total
Simulated Sources	502	198	700
Detected Sources	230	125	355

will be described by Lari et al. (2004) in order to obtain extragalactic source counts.

5.1 Flux Determination

The autosimulation process we use for flux determination, though relatively simple in principle, leads to several systematic effects which need to be carefully taken into account in order to understand how it can provide us with the best estimate of source fluxes. The analysis of its results on simulated sources will also allow us to test the goodness of our model and the reliability of the related signal reconstruction process. As described in Section 4, autosimulation involves simulating theoretical (i.e. noise-free) maps containing all (i.e. both real and simulated) sources of interest, then carrying out signal reconstruction on both theoretical and real sky maps, thus determining the theoretical ratio between peak

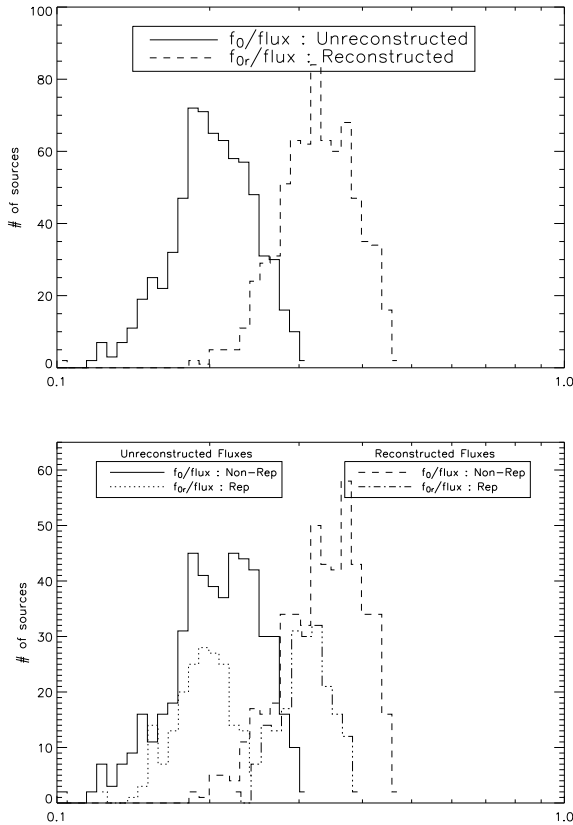


Figure 9. Peak/Total Flux Ratio for theoretical sky maps. Histogram distribution for both Unreconstructed and Reconstructed maps are given. Overall distributions are shown (top panel) together with those for non-repeated and repeated regions separately (bottom panel).

and total fluxes, and finally applying results determined on theoretical maps to correct real fluxes.

Figure 9 shows how mapping effects affect the relation between peak fluxes and total fluxes for both reconstructed and unreconstructed theoretical sky maps. Following the nomenclature adopted in Section 4, the histogram distribution of f_0/S_0 and f_{0r}/S_0 ratios are plotted for all sources (top panel) and separately for non-repeated and repeated regions (bottom panel). While the two distributions for non-repeated and repeated regions peak at slightly different values and thus have a (marginally) smaller width, the f_{0r}/f_0 ratio is remarkably similar, 1.61 being its mean value. This means that, according to our model, due to the short integration time adopted in observations with respect to the detector's response time constant, the measured flux, even in a noise-free image, will only equal 60% of the incident flux.

In order to correctly determine fluxes, however, one needs to make use of the employed detector's modeling and thus compare real fluxes with theoretical ones. By means of the f_s/f_0 histogram distribution, Figure 10 shows how real peak fluxes are systematically lower than theoretical ones, due to limits of the data reduction method and to the presence of noise. The width of the f_s/f_0 distribution is quite large, peaking at 0.83, showing a predictable narrowing of

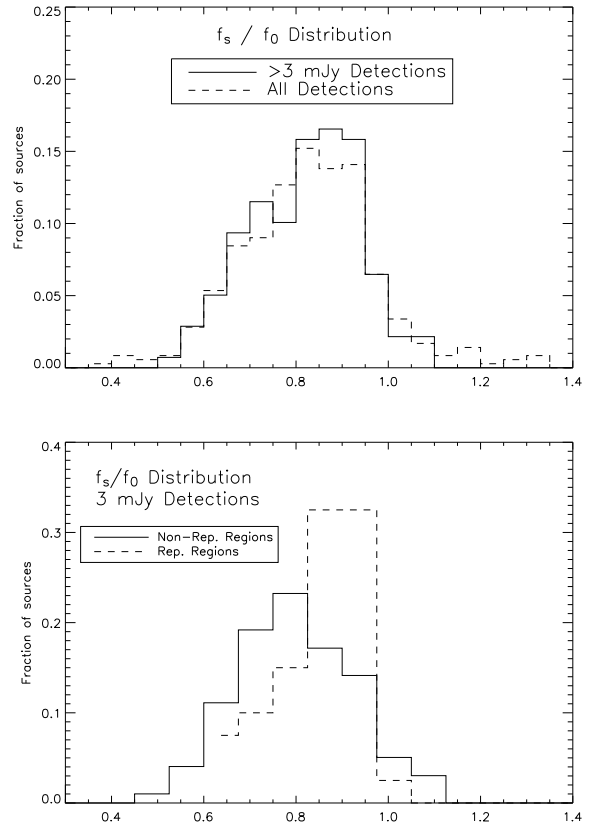


Figure 10. Real/Theoretical Peak Flux Ratio Distribution. The comparison between distributions for all detections and for bright source (> 3 mJy) detections is shown (top panel) together with the same comparison for detections in non-repeated and repeated regions (bottom panel).

the distribution at bright fluxes but on the whole a negligible dependence on flux (Figure 10, top panel, see also Figure 11). Conversely, values for non-repeated and repeated regions differ in a measurable way, mean values being 0.81 and 0.87, respectively. (Figure 10, bottom panel). The rms half-widths of the distributions are 0.17 and 0.12 in the two cases, respectively, which also provides an estimate of the photometric error in different regions, a quantity which will be assessed by different means in Section 8.

Figure 11 confirms the moderately small spread of the f_s/f_0 distribution and also shows the good linearity displayed by the f_s vs. f_0 relation, as long as a source is detected. Provided a suitable flux correction is applied to account for the f_s/f_0 distribution (see Section 5.2, this allows to confidently use our results at all the catalogue flux levels.

Figure 12 shows how well the signal reconstruction process carried out by the fitting procedure works at different fluxes. At it can be clearly seen, below a certain flux, f_s/f_{sr} systematically falls below the f_0/f_{0r} , that is goodness of signal reconstruction breaks down at the faint end. It was thus decided to use only unreconstructed fluxes in flux determination, so as to provide a flux estimate that would be reliable at all flux levels.

Finally, and most importantly, Figure 13 shows how total injected fluxes and peak real fluxes are related to each

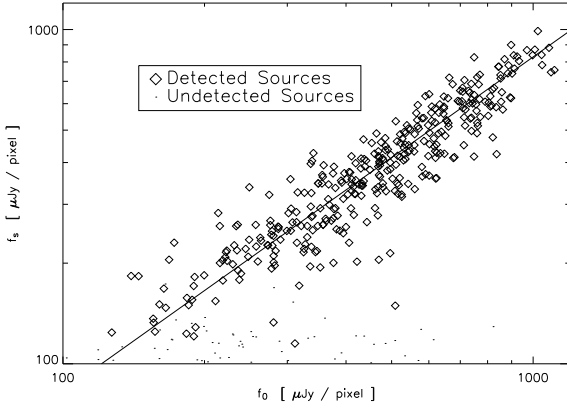


Figure 11. Real vs. Theoretical Peak Flux. The $f_s = 0.83 f_0$ line, corresponding to the 0.83 mean value of the f_s/f_0 ratio for detected sources, is also plotted.

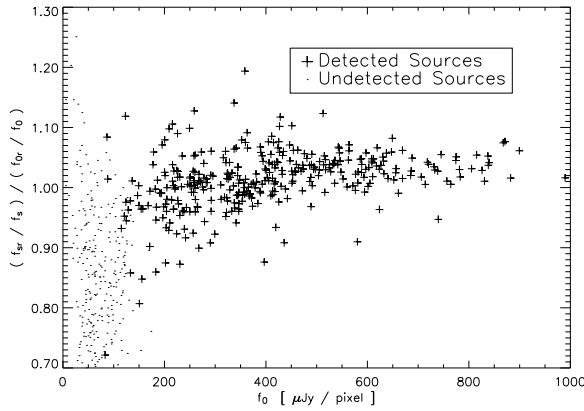


Figure 12. Signal reconstruction as function of real peak flux.

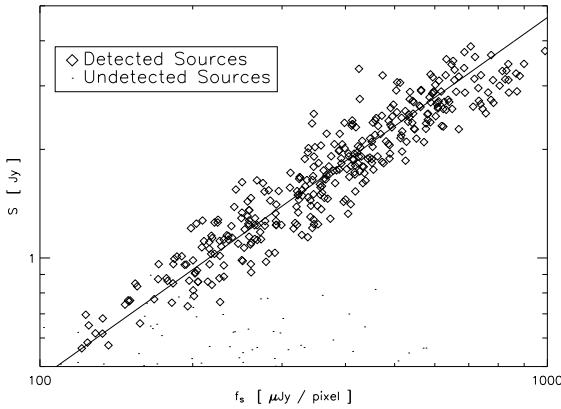


Figure 13. Total vs. Peak Flux. The $S = 4.64 f_s$ line, corresponding to the 4.64 mean value of the S/f_s ratio for detected sources, is also plotted.

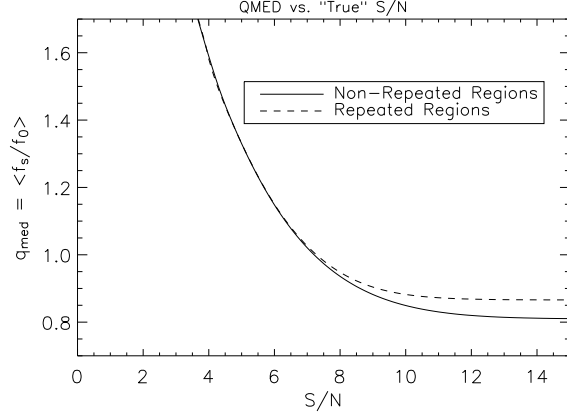


Figure 14. Flux Correction applied to Autosimulated Fluxes. The inverse of the correction factor, or q_{med} , is plotted against S/N for non-repeated and repeated regions.

other. The relation mimics the one between f_s and f_0 already shown in Figure 11, a linear relation with a reasonably small spread (the mean value of the S/f_s ratio being 4.64), warranting a reliable determination of total fluxes on the basis of measured peak fluxes.

5.2 Flux Correction

Systematic effects on flux estimates described in previous Section were modeled and taken into account using results from simulations and following Gruppioni et al. (2002). According to this approach, the correction to be applied to flux estimates obtained through autosimulation is derived from the so called g function, which describes the S/N -dependent distribution of the f_s/f_0 ratio. The g function is obtained as the combination of the intrinsic (i.e. high- S/N) g function, or g_0 function, and a term due to noise. First, the g_0 function is derived from the distribution of the f_s/f_0 ratio obtained for bright ($S > 3$ mJy) simulated sources (see Figure 10), by modeling and correcting for the small degree of incompleteness to be expected at such fluxes. Then convolution with a variable noise term is carried out to obtain the overall S/N -dependent g function. Finally, for each S/N value, the median f_s/f_0 ratio for detectable (i.e. $f_s > 5\sigma$) sources, or q_{med} , is computed. Autosimulated fluxes are then corrected by a factor $1/q_{med}$. This process was carried out separately for non-repeated and repeated regions, and the results are plotted in Figure 14. The two q_{med} curves asymptotically tend to the average f_s/f_0 values 0.81 and 0.87 determined for simulated sources in non-repeated and repeated regions, then virtually coincide and soar below $S/N \sim 7$, where $q_{med} \sim 1$.

It must be emphasized how all of the above applies to "relative" fluxes determined with respect to ISO LW3 standard sensitivity. In Section 9 the absolute flux calibration of our catalogue will be discussed on the basis of the comparison between measured and predicted MIR stellar fluxes and with respect to IRAS standard calibration.

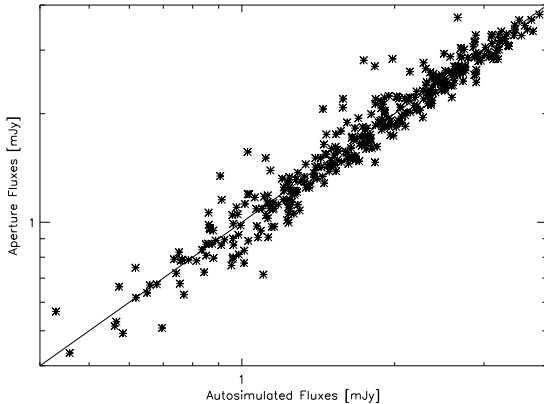


Figure 15. Autosimulated Fluxes vs. Aperture Fluxes

5.3 Autosimulation vs. Aperture Photometry

The performance of the autosimulation technique for flux determination described in Section 4 can also be assessed comparing the total fluxes obtained with this procedure with those obtained by means of ordinary aperture photometry.

The relation between these two quantities shows a good linearity for most sources, as it is shown for simulated sources in Figure 15. Plotted aperture fluxes were computed adopting an aperture of 6 arcsec radius and correcting both for the transients and for the 40 % of the instrumental PSF falling beyond this aperture. Such an aperture was chosen as the most reliable trade-off allowing to reliably include most of the source flux and lest of the background.

Only a few sources depart substantially from the 1:1 relation, with 94 % of sources with fluxes in accordance within 20 % and an overall rms deviation of 12 %. On the whole, our flux determination procedure is therefore consistent with conventional aperture photometry, provided a proper correction for PSF effects is applied.

5.4 Catalogue Flux Distribution

Flux distribution of catalogue sources is illustrated in Figure 16, with 50 % of the sources having fluxes greater than 1.65 mJy, 76 % greater than 1.2 mJy and 89 % greater than 1 mJy. As it can be clearly seen from the two separately plotted histograms, sources in non-repeated regions largely prevail in number down to about 1.5 mJy, at which flux their number per flux bin drops sharply. Conversely, the number of sources per flux bin in repeated regions continue to increase, if slowly, down to 1 mJy, where they already amount to about 50 % of the total number of sources. While detailed completeness estimates will be described by Lari et al. (2004), this plot seems to indicate that the catalogue is essentially complete up to ~ 1.5 mJy, and slightly fainter than that in repeated regions.

6 OPTICAL IDENTIFICATIONS

Identification of 15 μm sources was carried out on both archival and deep imaging obtained for this purpose at optical and near-infrared wavelengths. This provided optimal

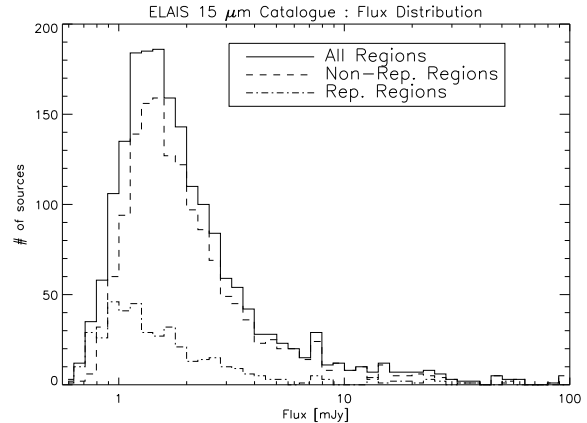


Figure 16. Histogram Flux Distribution of ELAIS Sources. All regions, non-repeated and repeated regions are plotted.

stellar discrimination as well as optical and near-infrared flux measurements over the whole large flux range probed by our catalogue, thus ultimately leading to a very reliable 15 μm photometric calibration (see Section 9).

The S1 field was surveyed in R down to $R \sim 23.0$ by La Franca et al. (2004) using the 1.5 Danish/ESO telescope. The N1 and N2 fields were surveyed in U , g' , r' , i' and Z down to 23.4, 24.9, 24.0, 23.2 and 21.9 respectively, as part of the Wide Field Survey (McMahon et al. 2001), using the Wide Field Camera at the Isaac Newton Telescope. Identifications of N1 and N2 15 μm sources based on maximum likelihood were obtained by (Gonzalez-Solares et al. 2004). Deep near-infrared imaging of areas around selected 15 μm sources was carried out by (Väisänen et al. 2002). Furtherly, USNO A2.0, GSC 2.2, Tycho-2, 2MASS All Sky Data Release and APM catalogues were cross-correlated with 15 μm sources so as to provide a list of tentative identifications. 15 μm contours were superimposed on DSS and 2MASS images as well as on new observational material, yielding diagnostic finding charts for extended, blended and disturbed sources.

Generally speaking, the identification based on deep optical imaging and automated source extraction and classification carried out with SExtractor was usually chosen, but archival material proved essential in dealing with bright sources, which appeared as saturated in deep observations, and in providing measurements for sources in the N3 or in small portions of the other three fields, where deep optical imaging had not been obtained. In particular, a positional difference of 6 arcsec, corresponding to 3 times the maximum estimated astrometric error of the 15 μm data reduction process (see Section 6), was adopted as a cut-off ensuring a safe identification.

The magnitude distribution of the sources identified as optical counterparts of 15 μm sources through this process is plotted in histogram form in Figure 17, showing a bimodal distribution whose two peaks are to be associated with stars and galaxies and sharply cutting-off at $R \sim 23$. The number of stars and total sources identified according to this criterion, is separately reported for the four fields in Table 5. About 90 % of 15 μm sources are assigned a robust optical association in N1 and N2 fields, while due to the shallower depth this fraction drops to about 80 % in the S1 and N3

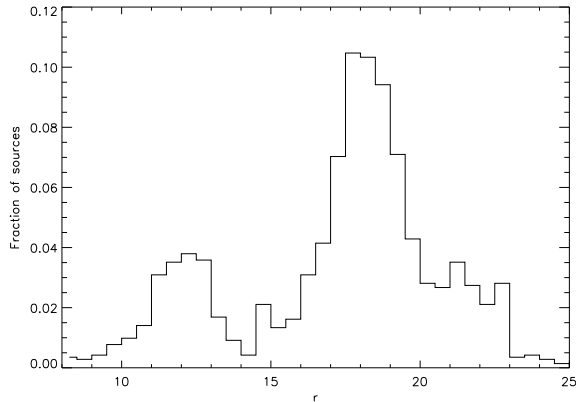


Figure 17. Magnitude distribution of optical IDs of $15\ \mu\text{m}$ sources. The two peaks at $r \sim 12$ and $r \sim 18$ are associated with Stellar and Extragalactic IDs, respectively.

Table 5. Some basic properties of the catalogue divided into different fields.

Field	Area [deg ²]	Sources #	Stars #	%	IDs #	%
S1	4.17	736	145	19.7	584	79.3
N1	2.84	490	121	24.7	441	90.0
N2	2.84	566	126	22.3	493	87.1
N3	1.00	131	29	22.1	103	78.6
Total	10.85	1923	421	21.9	1621	84.3

fields The average fraction of identified sources amount to 84.3%. Conversely, the statistics of stellar identifications is remarkably uniform between the 4 fields, with a 22% of stars and small field-to-field differences.

Figures 18 and 19 show how, at least down to the $15\ \mu\text{m}$ flux limit probed by ELAIS, it is furtherly possible to effectively discriminate between stars and galaxies solely on the basis of the comparison between optical and near-infrared magnitudes with $15\ \mu\text{m}$ fluxes, thus demonstrating the robustness of the identification process.

The optical identification process also allowed us to assess the astrometric accuracy achieved in $15\ \mu\text{m}$ data reduction independently of simulations, as it is described in Section 7.

7 ASTROMETRIC ACCURACY

Long-wavelength observations are frequently hampered by large astrometric errors, leading to severe difficulties in multi-wavelength identifications and thus physical studies of detected sources. In our case, astrometric errors can be considered as the combination of three error sources associated with the detector spatial sampling σ_s , the reduction method σ_r and the instrumental pointing accuracy σ_p , respectively.

The combination of the σ_s and σ_r terms, which we will hereafter indicate as σ_{s+r} , can be evaluated from simulations, comparing the injected positions of simulated sources with the corresponding detected positions, whereas the σ_p

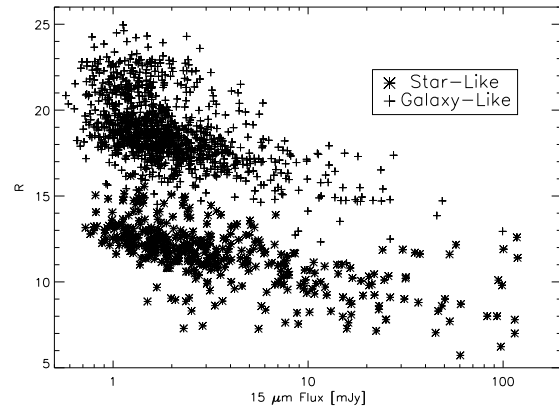


Figure 18. $15\ \mu\text{m}$ vs. R Flux-Flux Diagram of Identified Sources. Stellar and Extragalactic IDs are indicated.

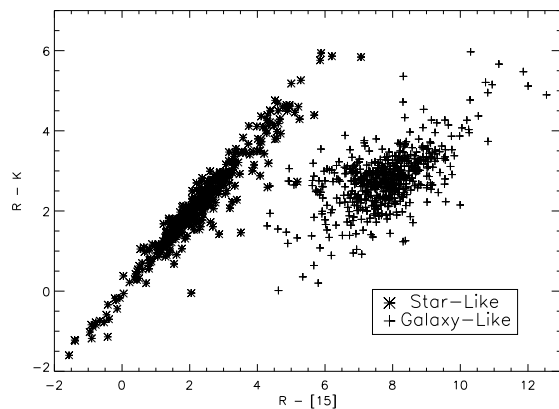


Figure 19. $R - K$ vs. $R - [15]$ Color-Color Diagram of Identified Sources. Stellar and Extragalactic IDs are indicated. The $[15]$ magnitude scale is defined in Equation 9.

term is given by the error on the rasters' astrometric offset, as derived in Section 3.6. The total astrometric error will then be given by

$$\sigma_{tot} = \sqrt{\sigma_{s+r}^2 + \sigma_p^2} \quad (6)$$

The overall distribution of the differences between injected and detected positions of simulated sources is shown in histogram form in Figure 20 for both non-repeated and repeated regions. Differences in RA and Dec are distributed in a remarkably similar way, which will allow us to use them together in the following statistical analysis, so as to increase our sample. About 75% simulated sources are detected within 1 arcsec of their injected positions and about 96% within 2 arcsec. Dependence of the σ_{s+r} on S/N can be evaluated binning simulated sources according to their S/N and computing the median positional difference of each bin. Thus one obtains the σ_{s+r} term as function of S/N . The σ_p term is obtained as the median value of astrometric offset errors per component reported in Table 3, that is 0.39 arcsec per component irrespectively of S/N . The total astrometric error per component is then computed through Equation 6. The results are illustrated in Figure 21, showing total astro-

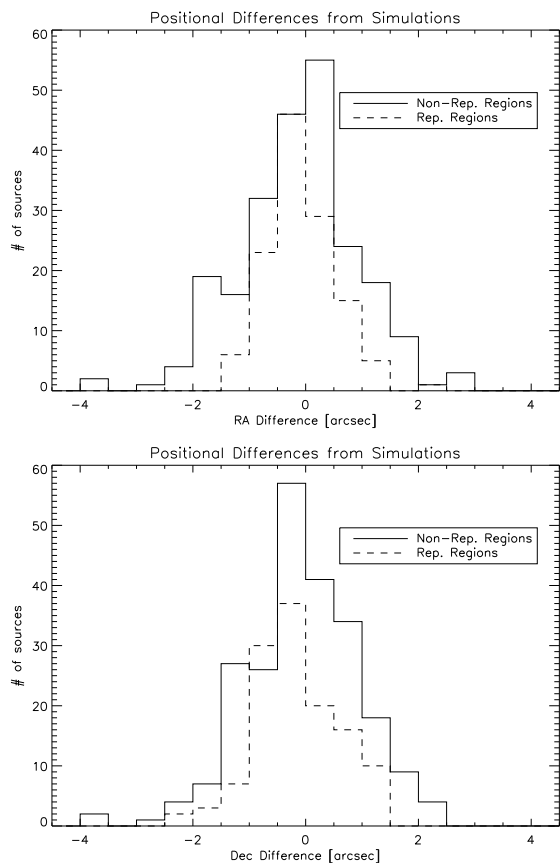


Figure 20. Sampling and Reduction Astrometric Error. Positional differences between injected and detected simulated sources in RA and Dec.

metric errors for sources detected both in non-repeated and repeated regions as function of S/N for $S/N < 30$. The astrometric accuracy turns out to be very good, errors being as low as 0.7 and 0.8 arcsec per component at the bright end in non-repeated and repeated regions, respectively. Catalogue astrometric errors can be estimated by fitting polynomials to the $\log \sigma_{tot}$ vs. $\log S/N$ curves for non-repeated and repeated regions derived from simulations. At the faint end, however, the errors computed in repeated regions unrealistically flatten below $S/N \sim 10$, due to the poor statistics following from the low number of simulated sources that are detected at low S/N levels. For this reason, we cross-checked the astrometric accuracy evaluated from simulations against an independent estimate based on optical identifications of catalogue sources (see Section 6). The same binning process described above was carried out on positional differences between catalogue sources and their optical counterparts, yielding the results plotted in Figure 21. The thus-derived σ_{tot} vs. S/N relation closely follows a straight line in the log-log plane at $5 < S/N < 20$, and closely resembles the one derived from simulations at $10 < S/N < 20$, confirming the overall robustness of the simulation process. It was thus decided to estimate catalogue astrometric errors by fitting a straight line to the $\log \sigma_{tot}$ vs. $\log S/N$ curves for non-repeated and repeated regions derived from optical identifications. At $S/N > 20$, other effects such as the widening of the instrumental PSF and the increase of the optical astro-

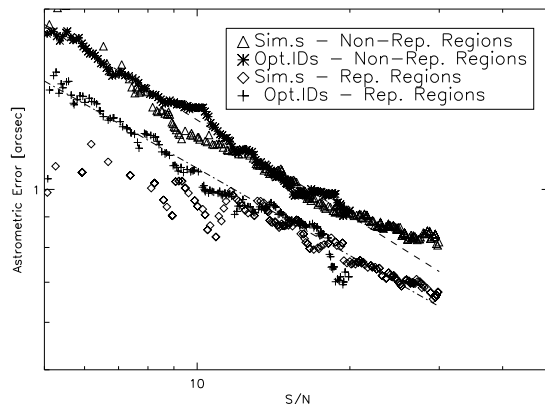


Figure 21. Astrometric Accuracy. Total astrometric errors per component as function of S/N in non-repeated and repeated regions. Polynomial fitting curves used for the evaluation of catalogue astrometric error are also indicated.

metric error begin dominating the astrometric error budget, and the astrometric error curve starts showing irregularities, so that linear fitting cannot be reliably assumed to describe the actual astrometric error. Accordingly, values obtained from simple extrapolation of the straight line obtained at $S/N < 20$ to higher S/N were truncated when they were deemed too optimistic, i.e. at the 0.8 and 0.7 arcsec values for non-repeated and repeated regions, corresponding to the extrapolated values for $S/N \sim 25$.

8 PHOTOMETRIC ACCURACY

Errors in flux determination using our method can mainly be attributed to two effects, namely the autosimulation process and the noise present on the sky maps. The first contribution can be estimated by computing the width of the f_s/f_0 distribution shown in Figure 10 for high S/N sources only, so as to evaluate the effects of the autosimulation process on relatively noise-free maps. At lower S/N , photometric errors arising from noise on the sky maps will combine with those arising from autosimulation. The overall error is thus given by

$$\left(\frac{\Delta S}{S}\right)^2 = \Delta\left(\frac{f_s}{f_0}\right)^2 + \left(\frac{\sigma_{map}}{f_s}\right)^2 = \Delta\left(\frac{f_s}{f_0}\right)^2 + \left(\frac{1}{S/N}\right)^2 \quad (7)$$

where $\Delta(f_s/f_0)$ is the width of the f_s/f_0 distribution as measured for high S/N sources for non-repeated regions and repeated regions separately, and σ_{map} is the noise as measured at each source position on the sky map. The first term is a constant, about 0.15 and 0.11 for non-repeated and repeated regions, respectively. This term dominates the photometric error budget at high S/N , whereas the importance of the second term increases when S/N decreases. Photometric errors estimated using Equation 7 are shown in Figure 22. The values for $S/N \sim 10$ are 0.18 / 0.15 for non-repeated / repeated regions, while they increase to 0.25 / 0.23 for $S/N \sim 5$.

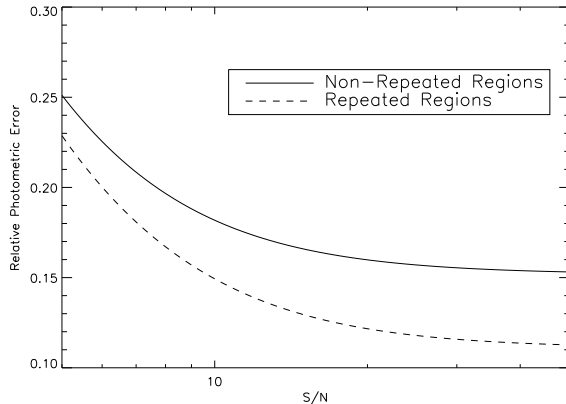


Figure 22. Relative photometric error as function of S/N as given by Equation 7 for non-repeated and repeated regions.

9 PHOTOMETRIC CALIBRATION

The standard sensitivity of ISO LW3 channel is of 1.96 ADU/Gain/s/mJy, which can be used to calibrate our catalogue fluxes. However, given the large sample at our disposal, the accuracy of such photometric calibration can be tested against the independently determined IRAS standard photometric calibration by studying detected sources with stellar counterparts. Aussel (2004) performed a detailed study of mid-infrared emission from stars, using large samples drawn from IRAS Faint Source Catalog with counterparts in the 2MASS and Tycho-2 (Høg et al. 2000) catalogues. In the two cases, it is found that the $J - K$ and $B - V$ colors of stars are extremely well correlated with the $K - [12]$ and $B - [12]$ colors, respectively, where $[12]$ is a magnitude scale constructed from IRAS $12\ \mu\text{m}$ flux, following the prescriptions of Omont et al. (1999). This relation allows to accurately predict the IRAS $12\ \mu\text{m}$ flux of a star, provided that its J and K (or B and V) are known and that $J - K$ (or $B - V$) are within certain limits. Stellar atmosphere models (Lejeune et al. 1998) show that such color criteria select stellar spectral types for which the ratio between the $15\ \mu\text{m}$ flux and the $12\ \mu\text{m}$ flux is essentially constant. Thus, if one has access to a substantial number of optical and/or near-infrared counterparts to $15\ \mu\text{m}$ sources, it is possible to use the correlations by Aussel (2004) to predict the $15\ \mu\text{m}$ fluxes of ISO-detected stars and compare them to the measured values. Such a comparison then allows to investigate possible systematic differences between the two sets of fluxes, which should be attributable to discrepancies between the independently established IRAS and ISO calibrations. Given the tighter nature of the near-infrared/mid-infrared correlation over a wide range of fluxes with respect to the optical/mid-infrared one, it was decided to use the former, that is expressed by

$$K - [15] = 0.044 + 0.098 (J - K), \quad (8)$$

where $[15]$ is a magnitude scale defined as

$$[15] = 3.202 - 2.5 \log (S_{15\ \mu\text{m}} [\text{mJy}]), \quad (9)$$

to compute predicted fluxes. 2MASS All Sky Release fluxes were used for the majority of the sources together with fluxes determined for fainter sources as part of the near-infrared

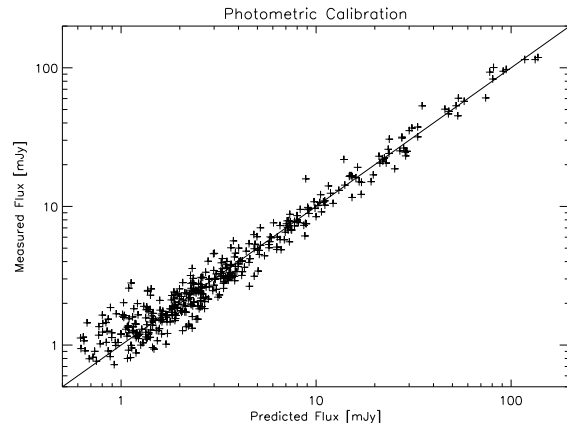


Figure 23. Photometric calibration. Measured vs. Predicted $15\ \mu\text{m}$ Stellar Fluxes. The 1.0974 correction factor to measured fluxes is here already taken into account, and the one-to-one relation is also plotted.

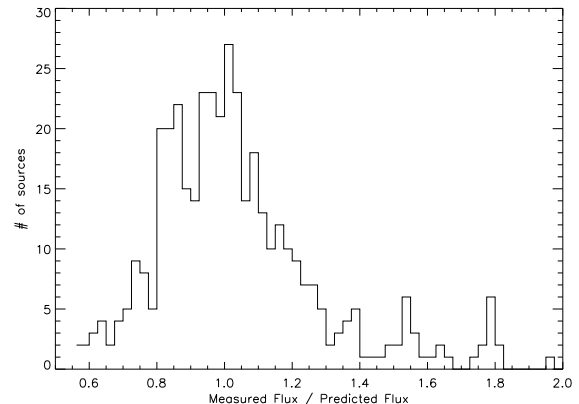


Figure 24. Photometric calibration. Histogram Distribution of Measured / Predicted $15\ \mu\text{m}$ Stellar Flux Ratio. The 1.0974 correction factor to measured fluxes is here already taken into account.

follow-up program to ELAIS observations (Väisänen et al. 2002). In Figure 23 measured fluxes are plotted against predicted ones for all 408 sources with reliable stellar identification and near-infrared magnitudes, showing the remarkable linearity and the small spread of the relation over a wide range of fluxes. Figure 24 shows the histogram distribution of the measured/predicted flux ratio. Reducing the sample to the 300 sources with a $S/N > 10$ yields an average predicted/measured ratio of 1.0974 with a standard deviation of 0.0121. The difference between measured and predicted fluxes is significant at ~ 8 sigma, suggesting the presence of systematic effects in either the IRAS or ISO calibration process. Disentangling the effects leading to such a discrepancy would involve the reduction of a wide set of IRAS-detected sources observed by ISO using our method. Given the substantial amount of work that would be needed for this purpose, it was decided to simply correct our catalogue fluxes by a constant 1.0974 factor to put them on the IRAS scale. However, while this choice was taken for the sake of compati-

bility of our results with studies adopting the IRAS flux scale (and particularly IRAS-based source counts and luminosity functions), this is not to indicate that IRAS calibration is more secure than ISO's. In fact, results from data reduction of deep ISOCAM surveys in the Lockman Hole using the LARI Method (Fadda et al. 2004) favour the ISO calibration. On the basis of stellar atmosphere models applied to a smaller number of stars and deep multi-band imaging, the authors find that model predictions agree with 15 μm fluxes determined following ISO calibration.

10 THE CATALOGUE

The ELAIS 15 μm Final Analysis Catalogue (Version 1.0) contains 1923 sources detected with a S/N greater than 5 in the (RA-ordered) four fields S1, N3, N1 and N2, totalling an area of 10.18 deg^2 . For each entry, the catalogue reports astrometric and photometric information, optical identification and a number of ancillary flags. The entries are as detailed in the following:

- **Name** : IAU source name constructed from Right Ascension and Declination;
- **RA (J2000)** : Right Ascension at epoch J2000 in both decimal and sexagesimal angular units;
- **Dec (J2000)** : Declination at epoch J2000 in both decimal and sexagesimal angular units;
- **Total Flux** : source total flux obtained from autosimulation or aperture photometry (see "Aperture" below), expressed in mJy;
- **Peak Flux** : source peak flux measured on unreconstructed maps, expressed in $\mu\text{Jy/pixel}$;
- **S/N** : signal-to-noise ratio measured on unreconstructed maps
- **Astrometric Error** : Astrometric error as determined from Equation 6
- **Photometric Error** : Photometric error as determined from Equation 7
- **Aperture** : aperture photometry flag, 0 for sources whose flux was estimated through autosimulation and 1 for sources on which aperture photometry was preferred (see Section 4);
- **Optical ID** : optical identification as described in Section 6. S stands for star, G for galaxy and * for unidentified source. A further D flags a particularly dubious (non-)identification.

A sample of the catalogue, which will shortly become available at <http://astro.imperial.ac.uk/~vaccari/elais>, is shown in Table 6. Some of the data on the sources are also contained within the ELAIS band-merged catalogue by Rowan-Robinson et al. (2003).

11 CONCLUSIONS

A technique for ISO-CAM/PHOT data reduction, the LARI method, was variously refined and applied to ELAIS 15 μm observations. The mathematical model for the detector's behaviour is the same as originally presented in Lari et al. (2001), but thanks to various improvements, and particularly to a new Graphical User Interface, the method is now

more robust and, most importantly, quicker and easier to apply to large datasets. Its application, in the new form, to the four fields composing the dataset (including a re-reduction of S1 observations already presented in Lari et al. (2001)) has produced a catalogue of 1923 sources spanning the 0.5 – 100 mJy range, detected with a S/N greater than 5 over a total area of 10.85 deg^2 . Optical identification of 15 μm sources has been carried out on heterogeneous optical and near-infrared imaging material, allowing to determine a robust association for about 85 % of the sources and identify 22 % of them as bona fide stars, further demonstrating the reliability of our data reduction process.

The evaluation of the catalogue's quality has been carried out through both accurate simulations and multi-wavelength identification. The astrometric accuracy is of order 1 arcsec in both RA and Dec for $S/N > 10$, while it increases up to about 2 arcsec in both RA and Dec for $S/N \sim 5$, and somewhat better for sources detected in higher-redundancy sky regions. The photometric accuracy is estimated to be below 25 % over the whole range of fluxes and redundancy levels probed by our catalogue, and better than 15 % for $S/N > 10$ sources.

The comparison of measured stellar fluxes with fluxes estimated on the basis of stellar atmosphere models calibrated on IRAS data and on near-infrared photometry allowed to achieve an IRAS/ISO relative photometric calibration. An IRAS/ISO relative calibration factor of 1.0974 ± 0.0121 was determined, shedding doubts on the goodness of the two independently determined calibrations at the 10 % level. For lack of a simple way to identify error sources in IRAS and/or ISO calibration process, it was decided to put our catalogue on the more commonly used IRAS flux scale.

In a forthcoming paper (Lari et al. 2004) completeness estimates and extragalactic source counts from this catalogue will be presented, covering the crucial flux range 0.5 – 100 mJy between ISOCAM 15 μm Deep Surveys and IRAS All Sky Survey.

ACKNOWLEDGMENTS

This paper is based on observations with ISO, an ESA project with instruments funded by ESA Member States (especially the PI countries: France, Germany, the Netherlands and the United Kingdom) and with the participation of ISAS and NASA.

The ISOCAM data presented in this paper were analysed using CIA, a joint development by the ESA Astrophysics Division and the ISOCAM Consortium. The ISOCAM Consortium is led by the ISOCAM PI, C. Cesarsky.

This work was partly supported by the "POE" EC TMR Network Programme (HPRN-CT-2000-00138).

REFERENCES

- Aussel H., Cesarsky C.J., Elbaz D., Starck J.L., 1999, *A&A*, 342, 313
- Aussel H., 2004, in preparation
- Bertin E., Dendenfeld M., Moshir M., 1997, *A&A*, 323, 685
- Cesarsky C.J. et al., 1996, *A&A*, 315, L32
- Désert F.X. et al., 1999, *A&A*, 342, 363

Table 6. A sample portion of ELAIS 15 μ m Final Analysis Catalogue. Source IAU Name, Right Ascension and Declination at J2000 epoch in sexagesimal formats, Total and Peak Flux, Signal-To-Noise Ratio, Astrometric and Photometric Errors, Aperture Flag. Note that a few columns described in text were dropped for the sake of brevity.

Name	RA (J2000)	DEC (J2000)	Total F.	Peak F.	<i>S/N</i>	Astr. E.	Phot. E.	Ap.
	hr min sec	deg min sec	mJy	μ Jy		arcsec	mJy	
ELAISC15_J143048.92+332830.08	14 30 48.9265	33 28 30.0837	1.2203	187.52	6.375	1.657	0.266	0
ELAISC15_J143053.24+333119.52	14 30 53.2422	33 31 19.5201	4.2931	649.40	18.421	0.944	0.691	0
ELAISC15_J143059.16+332215.08	14 30 59.1625	33 22 15.0859	3.0696	565.34	16.526	1.000	0.501	0
ELAISC15_J143112.10+325625.87	14 31 12.1003	32 56 25.8750	1.6166	166.20	5.266	1.834	0.392	0
ELAISC15_J143116.96+331957.83	14 31 16.9618	33 19 57.8304	3.1798	657.70	27.828	0.700	0.370	0
ELAISC15_J143116.99+332903.79	14 31 16.9954	33 29 3.7930	1.3766	296.39	12.327	0.980	0.189	0
ELAISC15_J143122.40+332036.07	14 31 22.4041	33 20 36.0725	2.2152	356.15	10.501	1.272	0.396	0
ELAISC15_J143123.57+330517.23	14 31 23.5781	33 5 17.2354	57.3303	11957.87	365.708	0.800	8.693	0
ELAISC15_J143125.36+331348.76	14 31 25.3603	33 13 48.7608	26.3799	1795.13	53.649	0.800	4.029	1
ELAISC15_J143131.33+330143.80	14 31 31.3313	33 1 43.8084	6.7570	958.24	30.352	0.800	1.048	0
ELAISC15_J143135.38+333224.62	14 31 35.3831	33 32 24.6235	0.8125	122.88	5.278	1.477	0.178	0
ELAISC15_J143135.47+325456.62	14 31 35.4741	32 54 56.6245	1.6331	301.73	9.053	1.376	0.306	0
ELAISC15_J143137.69+325453.32	14 31 37.6931	32 54 53.3249	2.5355	495.93	14.764	1.062	0.421	0
ELAISC15_J143138.44+332808.85	14 31 38.4461	33 28 8.8581	1.4309	274.79	7.864	1.483	0.283	0
ELAISC15_J143140.70+330316.82	14 31 40.7051	33 3 16.8265	3.6781	747.97	23.415	0.831	0.579	0
ELAISC15_J143142.01+331003.66	14 31 42.0114	33 10 3.6686	1.6108	269.70	8.391	1.433	0.310	0
ELAISC15_J143143.08+325301.48	14 31 43.0892	32 53 1.4801	1.2484	249.18	5.679	1.762	0.290	0
ELAISC15_J143143.58+333200.05	14 31 43.5875	33 32 0.0592	2.4374	386.42	14.690	1.065	0.405	0
ELAISC15_J143143.69+330133.41	14 31 43.6981	33 1 33.4117	2.4854	393.08	12.373	1.166	0.427	0
ELAISC15_J143143.86+333119.96	14 31 43.8619	33 31 19.9622	0.9966	200.88	6.450	1.647	0.216	0
ELAISC15_J143149.61+330212.86	14 31 49.6144	33 2 12.8683	2.7584	404.89	14.698	1.064	0.458	0
ELAISC15_J143155.98+330138.26	14 31 55.9881	33 1 38.2622	1.5529	263.79	7.163	1.558	0.320	0
ELAISC15_J143156.34+325138.33	14 31 56.3402	32 51 38.3395	3.8175	811.95	17.343	0.975	0.619	0
ELAISC15_J143159.54+325439.10	14 31 59.5441	32 54 39.1004	1.3582	232.94	6.381	1.656	0.296	0
ELAISC15_J143201.02+331525.84	14 32 1.0279	33 15 25.8460	2.0073	342.84	9.346	1.353	0.372	0

Elbaz D. et al., 1999, *A&A*, 351, 37
Fadda D. et al., 2004, in preparation
Franceschini A. et al., 1988, *MNRAS*, 233, 175
Genzel R. and Cesarsky C.J., 2000, *ARA&A*, 38, 761
González-Solares E. et al., 2004, *MNRAS*, submitted, astro-ph/0402406
Gregorich D.T. et al., 1995, *AJ*, 110, 259
Gruppioni C., Lari C., Pozzi F., Zamorani G., Franceschini A., Oliver S., Rowan-Robinson M., Serjeant S. 2002, *MNRAS*, 335, 831
Hacking P., Houck J.R., Condon J.J., 1987, *ApJ*, 316, 15
Høg E. et al., 2000, *A&A*, 355, 27
Kessler M.F. et al., 1996, *A&A*, 315, L27
Lari C. et al., 2001, *MNRAS*, 325, 1173
La Franca F. et al., 2004, *AJ*, accepted, astro-ph/0403211
Lari C. et al., 2003, *ESA SP-511*, 349
Lari C. et al., 2004, in preparation
Lejeune T., Cuisinier F., Buser R., 1998, *A&ASS*, 130, 65
Lemke D. et al., 1996, *A&A*, 315, L64
Lonsdale C.J. et al., 1990, *ApJ*, 358, 60
Lonsdale C.J. et al., 2003, *PASP*, 115, 897
Manners J.C. et al., 2003, *MNRAS*, 343, 293
McMahon R.G. et al., 2001, *New Astronomy Review*, 45, 97
Neugebauer G., Habing H. J., van Duinen R. et al., 1984, *ApJ*, 278, L1
Okumura K., 1998, *ISOCAM PSF Report*, available at http://www.iso.vilspa.esa.es/users/expl_lib/CAM_list.html
Okumura K., 2000, *ISOCAM Field Distortion Report*, available at

http://www.iso.vilspa.esa.es/users/expl_lib/CAM_list.html
Omont A., Ganesh S., Alard C., Blommaert J.A.D., Cailaud B. et al., 1999, *A&A*, 348, 755
Oliver S., Rowan-Robinson M. et al., 2000, *MNRAS*, 316, 749
Ott S., Gastaud R., Ali B., Delaney M., Miville-Deschênes M.-A., Okumura K., Sauvage M., Guest S., 2001, *ASP Conf. Ser.* 238, 170
Pozzi F. et al., 2003, *MNRAS*, 343, 1348
Rowan-Robinson M. et al., 1984, *ApJ*, 278, 7
Rowan-Robinson M. et al., 1991, *Nature*, 351, 719
Rowan-Robinson M. et al., 2003, *MNRAS*, accepted, astro-ph/0308283
Saunders W. et al., 1991, *Nature*, 349, 32
Schlegel D.J., Finkbeiner D.P., Davis M., 1998, *ApJ*, 500, 525
Serjeant S., Oliver S., Rowan-Robinson M. et al., 2000, *MNRAS*, 316, 768
Soifer B.T. et al., 1984, *ApJ*, 278, 71
Soifer B.T., Houck J.R., Neugebauer G., 1987, *ARA&A*, 25, 187
Starck J.L., Aussel H., Elbaz D., Fadda D., Cesarsky C., 1999, *A&AS*, 138, 365
Väisänen P. et al., 2002, *MNRAS*, 337, 1043